Engineering Structures 360 (2026) 122675

Contents lists available at ScienceDirect

Engineering Structures

journal homepage: www.elsevier.com/locate/engstruct

Evaluating cracking behaviours in precast prestressed alkali-activated concrete (AAC) bridge decks using ultrasonics-based damage indicators

Hao Cheng [a,*], Shizhe Zhang [a,b], Zhenxu Qian [a], Guang Ye [a], Yuguang Yang [a]

[a] Faculty of Civil Engineering and Geosciences, Delft University of Technology, Stevinweg 1, Delft 2628 CN, the Netherlands
[b] Renewi Mineralz & Water, Vlasweg 12, Moerdijk 4782 PW, the Netherlands

ARTICLE INFO

Keywords:
Alkali-activated concrete (AAC)
Precast concrete bridge
Damage indicators
Embedded piezoelectric sensor
Ultrasonic pulse velocity (UPV)
Direct wave interferometry

ABSTRACT

Alkali-activated concrete (AAC) is a sustainable alternative to ordinary Portland cement concrete, but its large-scale structural performance remains insufficiently understood, particularly in terms of long-term durability. To ensure safe application, continuous monitoring of AAC structures is essential. This paper develops and validates ultrasonic-based damage indicators (DIs) intended to support future lifetime monitoring of precast AAC bridge members. Full-scale laboratory tests were performed on two prestressed AAC beams and a solid slab consisting of three beams with embedded piezoelectric sensors. Active ultrasonic measurements collected throughout loading were processed to derive two DIs: (1) reduction in waveform coherency using direct wave interferometry to indicate crack initiation, and (2) relative wave velocity obtained from an arrival-time picker to track crack propagation. The waveform coherency-based DI consistently identified the onset of cracking at or even before the first visible cracks appeared in digital image correlation (DIC) images, while the velocity-based DI provided a qualitative measure of crack propagation and orientation. Both indicators responded sensitively once degradation developed, enabling early warning of structural deterioration. The validated DIs are intended to inform the development of a lifetime monitoring scheme on a pilot precast AAC bridge on a Dutch national road. This study also provides a practical pathway toward risk-informed operation and broader adoption of AAC in bridge applications.

1. Introduction

Cement production is inevitably accompanied by high energy demand and significant CO_2 emissions [1]. Today, cement production accounts for about 5% of global fossil CO_2 emissions [2]. The increasing significance of sustainability in engineering practices underscores the need for the cement and concrete industry to meet the sustainability criteria in infrastructure projects. Possible solutions for reducing the CO_2 emissions for the concrete industry involve developing new binding materials for concrete, i.e., belite cement [3,4], calcium sulfoaluminate (CSA) cement [5,6], and alkali-activated binders [7,8], which can partially substitute conventional cement. Among them, concrete based on alkali-activated binders, or alkali-activated concrete (AAC), demonstrates comparable or sometimes even better performance in comparison to conventional Portland cement concrete [9–11]. AAC also has the potential to convert various industrial by-products and waste streams into useful construction materials [12].

However, scaling-up AAC application from laboratory-scale specimens to large-scale structural members with complex stress distributions, such as precast prestressed bridge components, remains rare due to limited knowledge of its structural performance, insufficient construction experience and the absence of design guidelines. Furthermore, uncertainties persist regarding its response to realistic long-term loading conditions, including prestressing, self-weight, traffic loads, time-dependent deformations and environmental changes. These knowledge gaps hinder the broader application of AAC in practice, calling for further studies.

To address these knowledge gaps and promote application of AAC, an initiative was launched by the Provincial Government of Friesland in the Netherlands to use AAC for structural applications. The main aim of this initiative is to study, design, and ultimately construct the first precast solid slab bridge with AAC on a national road in the Province of Friesland. To facilitate informed design decisions regarding the identified knowledge gaps and to mitigate the risk of structural failure, a set of full-scale laboratory failure tests was designed to justify design choices. In both laboratory tests and the construction of the actual bridge, a

* Corresponding author.
E-mail address: haojaysonshing@gmail.com (H. Cheng).

https://doi.org/10.1016/j.engstruct.2026.122675
Received 11 November 2025; Received in revised form 17 March 2026; Accepted 4 April 2026
Available online 18 April 2026

refined monitoring program was developed to collect data on structural responses and damage evolution. The information is essential for the design, construction, and lifetime maintenance process.

To facilitate the long-term monitoring process, we propose several damage indicators (DIs) through laboratory tests using structural health monitoring (SHM) techniques to bridge the gap between SHM data and the structural behaviour of full-scale AAC bridge components. The obtained DIs will be further utilized in the monitoring of the real bridge to mitigate the risk of structural failure. This provides material scientists and structural engineers with direct insight into the safe application of AAC as structural members in conjunction with SHM techniques. It is noteworthy that certain indicators have been proposed for the long-term monitoring of the global behaviour of bridges made of conventional concrete, such as the visual inspection-based crack width indicator [13–15] and the strain measurement-based neutral axis indicator [16]. Nonetheless, the visual inspection-based crack width indicator can only detect cracks once they are visible and cannot capture the progressive deterioration of the structure. Furthermore, the strain measurement-based neutral axis indicator may identify issues only after significant structural changes have occurred, which is not well suited to the present application, as the formation of flexural cracks at critical cross sections is recognized as the first step towards structural failure [17].

In this paper, we propose and evaluate two ultrasonic damage indicators, namely a waveform-coherency-based correlation coefficient (*CC*) and a relative wave-velocity indicator derived from ultrasonic pulse velocity (UPV), for an AAC bridge constructed using a specific method, namely a solid-slab deck with embedded precast beams. The construction method is commonly used in the Netherlands with unique precast beam cross sections. Dedicated DIs for this type of bridge deck are developed based on full-scale laboratory tests to capture the progressive deterioration of the structure. For simplicity, we refer to this bridge deck as a precast solid slab in the rest of the paper. The use of *CC*- and UPV-based indicators has been previously investigated for SHM of conventional concrete; however, their interpretation in terms of serviceability and ultimate limit states and their applicability to full-scale prestressed AAC slab-bridge systems have not yet been established. The present work addresses this gap by tracking the evolution of these indicators in full-scale AAC members and linking them to crack initiation and propagation as well as to global structural performance. The methodology for the DIs, including the objectives and signal processing techniques, is introduced in Section 2 (with a concise review of existing approaches in Section 2.1). The geometries of the bridge members and the sensor layouts for laboratory tests are detailed in Section 3. The experimental setup and measurement plan for sensors are presented in Section 4, while Section 5 provides validation of the DIs.

2. Methodology for damage indicators

2.1. Roles of damage indicators and selection of structural health monitoring methods

For a properly designed structural member without over-prestressing, the formation of flexural cracks at critical cross sections, which leads to stiffness degradation at the cross section and causes irreversible damage, is recognized as the first step toward structural failure in most failure tests on structural members [17]. Based on this consideration, the timely detection of crack initiation serves as a key indicator of the proper functionality of a prestressed member.

While crack initiation in concrete is a useful serviceability indicator, it should be supplemented with a failure-process-related indicator to ensure robust structural assessment, as crack initiation in real bridges is influenced by factors such as concrete shrinkage, thermal effects, and loading conditions. Therefore, after cracks have initiated, it is also crucial to track crack propagation to provide warnings for:

1. Deterioration of flexural behaviour at the critical cross section of the slab strip.
2. Potential brittle shear failure induced by shear crack propagation in the shear-critical zone of the slab strip [18].

In the context of precast solid slab bridges, we focus on monitoring two key structural changes throughout the service life of the bridge: crack initiation and crack propagation. These represent two levels of structural deterioration. Crack initiation indicates a reduction in durability, as cracks increase the risk of chloride, water, and oxygen intrusion, potentially leading to the corrosion of prestressing strands and rebars. Thus, it can serve as an indicator for the Serviceability Limit State (SLS). Crack propagation, on the other hand, directly contributes to the deterioration of structural responses and represents an irreversible sign of structural damage, making it an indicator related to damage progression toward the Ultimate Limit State (ULS).

Since crack initiation results in subtle changes in the concrete, detecting these changes requires an SHM method with sufficient sensitivity. To this end, we select the ultrasonic method, which is highly sensitive to material changes [19]. In contrast to conventional SHM methods such as strain gauges [20], fibre Bragg grating sensors [21], and distributed fibre optic sensors [22], the ultrasonic method offers a distinct advantage by extending monitoring beyond specific locations or sensor lines. Because it uses high-frequency elastic waves, the ultrasonic method is sensitive to wave propagation within a surrounding volume rather than restricting it to discrete points or predefined paths. When placed strategically at multiple locations, ultrasonic sensors can function as a network to monitor designated areas within the concrete. This broader coverage improves the ability of the method to detect changes and events across a larger section of the bridge.

Five main ultrasonic parameters are widely used in elastic wave-based concrete monitoring, including UPV, attenuation parameters (such as scattering-related and intrinsic-dissipation-related attenuation), nonlinear parameters, waveform coherency, and travel-time or velocity change. Here, 'waveform coherency' refers to an indicator of waveform similarity (as defined in Table 1 by Liu [26]), rather than the physical presence of coherent waves. Table 2 compares these parameters in terms of sensitivity to crack initiation, robustness to noise, and capability for macro-crack characterization. UPV is a conventional ultrasonic parameter widely used to assess concrete quality and detect macro-cracks in concrete [27,28]. However, several studies [29,30] have shown that UPV is generally not sensitive to crack initiation. This is because UPV is based on time-of-flight measurements, and small-scale changes in the medium often do not result in measurable variations in travel time due to resolution limits. On the other hand, this reliance on

Table 1
Comparison between the ultrasonic method and conventional SHM methods in monitoring the local region of concrete structures.

SHM method	Monitoring range	Spatial flexibility	Typical applicable range
Strain gauge-based method [20]	Restricted to discrete mounting points	Low	Localized strain monitoring at specific locations
Fibre Bragg grating (FBG)-based method [21]	Restricted to discrete installed points	Low	Localized strain and temperature monitoring at specific locations
Distributed fibre optic sensors (DFOS)-based method [22]	Quasi-continuous along the entire fibre path	Moderate	Distributed strain and temperature monitoring
Ultrasonic method [19]	Sensitive to elastic wave propagation within a surrounding volume, not limited to points or paths	High	Strain/stress [23], temperature [24], and damage [25] monitoring in critical regions of large concrete members

Table 2
Comparison of ultrasonic parameters in terms of sensitivity, robustness, and macro-crack characterization for monitoring local regions of concrete structures.

Parameter	UPV	Attenuation parameter	Nonlinear parameter	Waveform coherency	Velocity change
Sensitivity to crack initiation	Low	High	Very high	High	Moderate
Robustness to noise	High	Low	Low	Moderate	Moderate
Macro-crack characterization	Severity and direction	Severity	Severity	Severity	Severity

timing also makes UPV typically robust against random noise, which has little effect on arrival-time estimation. Compared with UPV, attenuation parameters are generally more sensitive to crack initiation and micro-cracks in concrete [30]. They can also be used to evaluate the severity of damage in a given region. However, attenuation generally provides only a qualitative assessment of macrocracks and does not yield information about crack location or orientation [31]. Moreover, because attenuation is calculated from amplitude or energy, it is highly sensitive to noise levels [32,33]. Nonlinear parameters, by contrast, are highly sensitive to microstructural changes in concrete [34]. Nevertheless, when applied to macrocrack scenarios, these parameters often exhibit high variability [35–37]. Furthermore, second- or third-harmonic amplitudes are often needed in the calculation of nonlinear parameters. These amplitudes are typically very low and easily influenced by noise [38]. Waveform coherency and velocity change are both derived using wave interferometry. Waveform coherency is generally highly sensitive to structural changes in the medium, such as cracking [39–41]. Velocity change, on the other hand, responds not only to structural changes [42] but also to stress [43] and temperature [44] variations. Consequently, measured velocity change typically reflects a coupled effect of these phenomena, which reduces its effectiveness for early damage detection, especially in regions where stress changes are present. When a macrocrack develops, waveform similarity decreases sharply, making both parameters useful for evaluating damage severity [45]. However, due to the complexity of scattered wave paths, they remain difficult to apply for determining crack location or direction.

To ensure timely detection of crack initiation, we employ waveform coherency as the indicator, as this parameter is highly sensitive to crack initiation and exhibits moderate robustness against noise. A wave interferometry technique, called the stretching technique [46], is used to evaluate waveform coherency through the correlation coefficient (*CC*), which is highly sensitive to minor changes in the medium [44]. The *CC* value is computed between each waveform and its own reference at the previous load step, so variations due to density or curing conditions are largely cancelled out and do not significantly affect the crack-induced reductions in waveform coherency. The stretching technique and its corresponding DI are introduced in Section 2.2. For detecting crack propagation, we adopt the UPV parameter as the indicator, as it can characterize macro-cracks, is robust to noise, and has the potential to reveal crack orientation, which is crucial for determining the failure mode. The UPV parameter is calculated based on the arrival-time picker. To eliminate the influence of spatial variations in absolute wave velocity on crack detection [47], a relative velocity, defined with respect to the unloaded reference state, is adopted in this study. The relationship between UPV and crack orientation, along with details of the arrival-time picker, is presented in Section 2.3.

2.2. Waveform coherency-based damage indicator for crack initiation

The initiation of cracks in concrete represents a subtle change in the material, which typically does not result in a significant change in wave velocity. However, the initiation of cracks within the scope of elastic waves can alter the wave path, leading to distortions in the received waveforms. These crack-induced distortions further reduce the similarity between the waveforms in the medium before and after cracking, which can be quantified using the *CC* of these two waveforms [48,49]. It should be noted here that *CC* indicates the waveform coherency, which is highly sensitive to subtle structural changes within the medium, and, according to previous research [50–52], the magnitude of *CC* reduction caused by crack initiation is generally greater than 0.1.

The *CC* value can be obtained using the stretching technique, which is a wave interferometry technique that compares two waveforms: one recorded before perturbation (u_{unp}) and one after perturbation (u_{per}) [46,53]:

$$CC(t_0,T,\alpha)=\frac{\int_{t_0}^{t_0+T}u_{\mathrm{unp}}(t')u_{\mathrm{per}}[t'(1-\varepsilon)]\,dt'}{\sqrt{\int_{t_0}^{t_0+T}u_{\mathrm{unp}}^2(t')dt'\int_{t_0}^{t_0+T}u_{\mathrm{per}}^2[t'(1-\varepsilon)]\,dt'}}\quad , \tag{1}$$

where *CC* is the correlation coefficient, ε represents the factor for stretching or compressing the signal, t_0 denotes the starting time of the time window, and T represents the duration of the time window. More information regarding the stretching technique can be found in the authors' previous article [54].

The stretching technique can be applied to either the early segment, known as direct wave interferometry (DWI) [43], or the later segment, termed coda wave interferometry (CWI) [50,55]. CWI offers heightened sensitivity to subtle changes compared to DWI, due to the longer wave path that accumulates these changes. However, this increased sensitivity is a double-edged sword, as it makes CWI more susceptible to environmental factors such as temperature fluctuations [44]. Considering the intended six-hour interval between measurements on the real bridge and the large temperature fluctuations expected during this interval, we apply the stretching technique to the early time window, which corresponds to DWI. While this approach sacrifices some sensitivity, it offers enhanced robustness against environmental variations.

2.3. Ultrasonic pulse velocity-based damage indicator for crack propagation

2.3.1. Relationship between cracks and velocity of elastic waves

The physical principle behind detecting cracks (including both visible and internal ones) through elastic wave velocity lies in the interaction between cracks and propagating waves. When a crack lies on the trajectory between the sender and receiver, the wave undergoes scattering and refraction during propagation. These interactions increase the effective travel time [56]. Assuming the sensor distance remains constant, the velocity, defined as distance divided by travel time, therefore decreases.

Beyond this basic principle, wave velocity in concrete is also strongly influenced by crack orientation [57,58]. For uniformly distributed, randomly oriented cracks, the effect is an essentially isotropic velocity reduction compared with the uncracked medium [59]. Such behaviour is often modelled using an isotropic effective medium, where crack density [60–62] and crack size (or aspect ratio) [59] are key parameters controlling the effective velocity. By contrast, structural cracks in concrete members develop in response to loading conditions, and their orientation is strongly dependent on the applied loading scheme. For example, cracks formed during a beam shear test are typically diagonal [63]. In these aligned-crack cases, velocity becomes anisotropic, depending on the propagation direction relative to the crack orientation. This anisotropy can be modelled by treating the cracked medium as a transversely isotropic effective medium, as proposed by Eshelby [64] and Hudson [65,66], where P-wave velocity is expressed as a function of the angle between the propagation direction and the crack normal. This relationship is shown in Fig. 1, originally plotted by Cheng [67]. As illustrated, velocity reaches a minimum when waves propagate

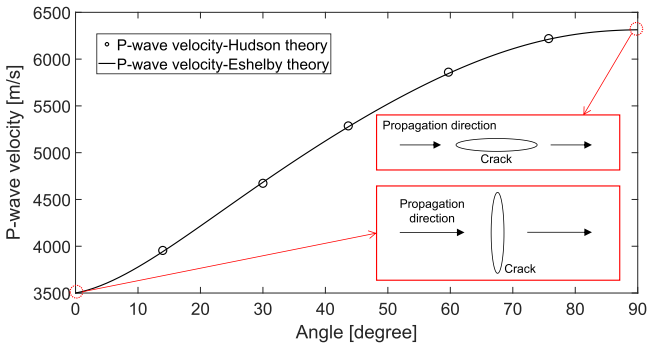

Fig. 1. Comparison of P-wave velocities in cracked medium as a function of angle for Hudson's and Eshelby's theories (replotted based on the result reported by Cheng [67]). The background medium is taken to be a Poisson solid with λ=μ= 39 GPa. The crack aspect ratio is 0.01 and the crack porosity is 0.005. Please note that velocity reduction also depends on crack aperture and wave frequency, i.e., dispersion effects, which are not shown here.

perpendicular to cracks and a maximum when they propagate parallel to them. Such behaviour reflects frequency-dependent transmission and scattering at cracks: waves incident perpendicular undergo stronger scattering and phase delay (and, under broadband excitation, additional dispersion and amplitude attenuation), yielding lower apparent velocities, whereas waves traveling parallel encounter less impedance and thus higher apparent velocities [68].

Importantly, these mechanisms also explain the evolution of velocity as cracks propagate under loading. With increasing crack density and aperture, scattering and phase delay effects intensify, producing a progressive velocity decrease along trajectories in the crack zone. At the same time, as cracks align with the stress field, velocity anisotropy becomes more pronounced: velocities decrease more significantly in directions perpendicular to the dominant crack orientation while remaining relatively higher in parallel directions. Consequently, temporal velocity changes not only indicate the presence of cracks but also provide insight into their progressive growth and orientation during loading. It should be noted that, in this study, crack propagation was not tracked in real time during loading. Instead, during monotonic loading, once a given load level was reached, the load was held constant to determine the crack level within the sensor network at that load step.

2.3.2. *Arrival-time pickers for the UPV technique*

The UPV technique is a conventional method for ultrasonic-based concrete monitoring [27]. The UPV procedure involves activating the actuator with a pulse, causing it to vibrate and generate elastic waves within the concrete medium. These waves propagate along a defined wave path and are detected by receivers placed at specific locations. A critical step in this process is accurately capturing the arrival time of the received signal. These data are essential for calculating pulse velocity, assuming a direct and linear path between the actuator and receiver. Precision in determining the arrival time is crucial, as it directly influences the reliability of the UPV results.

There are two arrival-time pickers commonly used in the literature: Hinkley criterion (HC) picker [69] and Akaike information criterion (AIC) picker [70]. The HC picker is based on the wave energy. For a signal S with the length of N, the HC value at n is defined by [69]:

$$HC(n) = \sum_{i=1}^{n} S_i^2 - \frac{nS_N}{\alpha N} \quad , \tag{2}$$

where S_N is the total energy of the signal and n ranges through all the samples in the signal. The factor α is to reduce a systematic delay of the global minimum of the modified partial energy of the signal which comes from subtraction of the trend. The point with the minimum HC value is selected as the onset point. The performance of HC picker is highly dependent on the value of factor α. In application, its value is usually chosen to fall within the range of 2–200 to ensure minimal delay [71].

The AIC picker, on the other hand, is based on the variance of the signal. This picker is believed to be more accurate than the HC picker [71]. For a signal S with the length of N, the AIC value at n is defined by [70]:

$$AIC(n) = n\log\{\mathrm{var}(S[1,n])\} + (N-n-1)\log\{\mathrm{var}(S[n+1,N])\} \quad , \tag{3}$$

where n ranges through all the samples in the signal. The point with the minimum AIC value is selected as the onset point. In contrast to the HC picker, the performance of AIC picker is significantly related to the selection of the time window. This picker should be operated within a time window of limited duration, characterized by a high signal-to-noise ratio (SNR) and clearly discernible arrival time [72]. Choosing a time window of much longer duration may result in an inaccurate onset point.

In this paper, we employ both the HC picker and the AIC picker for arrival time determination. Leveraging the insensitivity of the HC picker to time-window durations, we initially employ this picker to provide a rough estimate of the time-window range for arrival time, using the entire signal and setting α to 50. The established time-window range is subsequently used for precise onset time determination with the AIC picker.

3. Members and sensor layout

3.1. *AAC bridge members*

The AAC composite slab system typically consists of two parts: the prestressed precast beams, which serve as the load-bearing system and formwork during construction, and the cast-in-situ layer in-filling both between the beams and on top of the beams. The manufacturing process unfolds in two stages, beginning with the production of the precast beams in a prefabricated concrete factory. A total of 16 straight prestressing strands (nominal diameter 12.9 mm) were arranged in two layers. Of these, four strands were left unbonded over a length of 1000 mm from each end. FeP1860 strands were used, with a tensile strength of 1915 MPa and a 0.1% proof stress of 1694 MPa. The elongation at maximum load and at 0.1% proof stress was 5.95% and approximately 1.1%, respectively.

The strand and reinforcement layouts of the precast beam and the cast-in-situ topping layer are shown in Fig. 2. B500B ribbed reinforcement was used for the longitudinal reinforcement and stirrups. The stirrups were spaced variably within 1350 mm of each end and uniformly at 250 mm intervals along the remaining 4250 mm of the girder. The precast girders were designed elastically (fully prestressed) using the allowable-stress concept [73]. After casting at the precast plant, a prestress of approximately 16.3 MPa was applied to concrete by cutting the strands at 3 days. The girders were then cured under moist burlap and plastic foil. After around 31 days, the cast-in-situ infill layer was cast to connect the precast beams into a solid slab. The prestress eccentricity was 44.3 mm from the bottom surface before casting the in-situ topping layer and 149 mm after casting, respectively.

The mixture of self-compacting AAC used for the precast prestressed beam is outlined in Table 3. This mixture was first developed at Delft University of Technology and later scaled up and successfully produced on an industrial scale [74,75]. The AAC in the cast-in-situ topping layer consists of 400 kg of aluminosilicate precursor, 180 liters of liquid (including alkali activators) and 2.5 kg of admixtures per cubic meter. The average 28-day compressive strength of the AAC in the prestressed beam and in the cast-in-situ layer is 64.9 MPa [75] and 51.8 MPa [76], respectively.

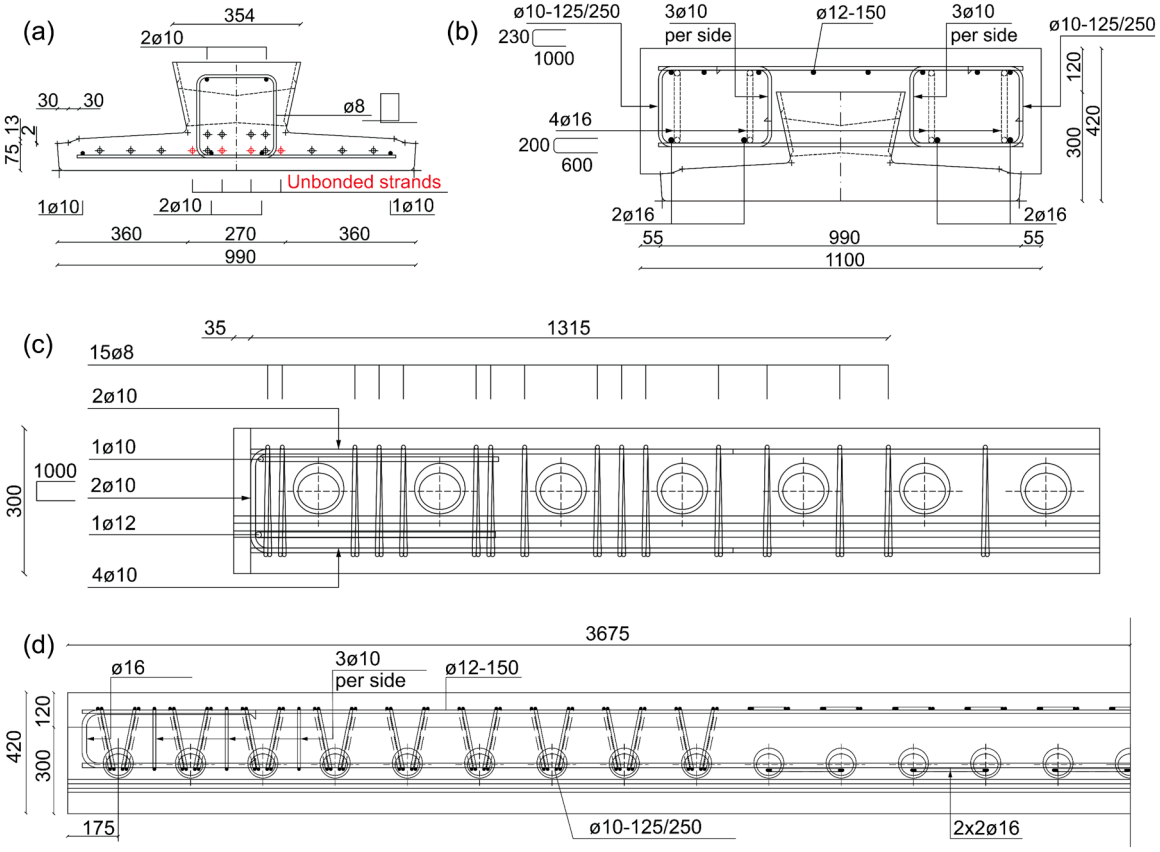

Fig. 2. Geometry, strand layout, and reinforcement layout of precast beam and cast-in-situ topping layer (unit: mm). (a) Cross-section and strand layout of precast beams. (b) Cross-section and reinforcement layout of cast-in-situ topping layer. (c) Shear reinforcement layout at the end of precast beams. (d) Shear reinforcement layout of the cast-in-situ topping layer.

Table 3
Mixture composition of the AAC used in the prestressed beam [74].

Materials	Content [kg/m^3]
Blast furnace slag	550.0
NaOH solution (50.0 wt%)	36.9
Sodium silicate solution (48.0 wt%)	80.4
Water	191.5
Admixture/Retarder	1.375
Sand 0/4 mm	762.2
Gravel 4/16 mm	675.0

3.2. Sensors

Given the prolonged utilization of ultrasonic sensors over the expected service life of the bridge, the selected sensor must be sufficiently robust for long-term service. Taking this factor into account, we opt for an embeddable piezoelectric sensor [77,78] for the long-term monitoring of the bridge.

The embeddable piezoelectric sensor comprises a d_{33} PZT patch, a waterproof copper package, and two protective marble blocks. The incorporation of marble blocks serves the critical purpose of shielding the delicate PZT. This sensor has a cylindrical shape with a diameter of 25 mm and a height of 20 mm. The centre frequency of this sensor is approximately 80 kHz [79]. The schematic illustration of the sensor is shown in Fig. 3(a). Notably, this sensor exhibits versatility by functioning as both an actuator and a receiver due to the reversibility of the piezoelectric effect. This dual functionality renders the sensor suitable for both passive and active monitoring applications [80]. Furthermore, the embedded nature of this piezoelectric sensor within the structure enhances its resilience to environmental changes. A photo of the embeddable piezoelectric sensor is depicted in Fig. 3(b).

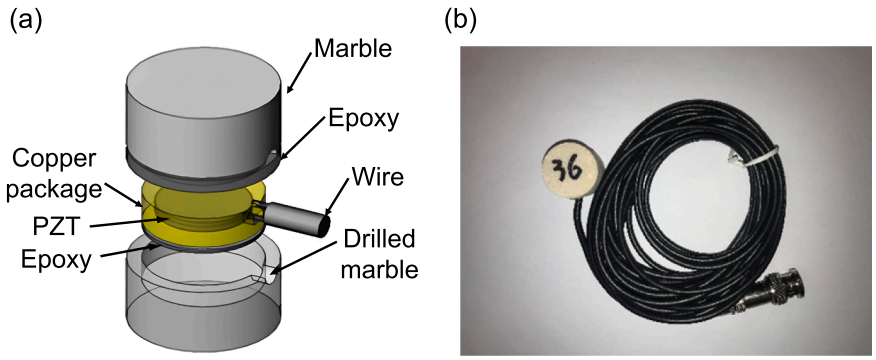

Fig. 3. Schematic and photo of an ultrasonic sensor used in this study. (a) Schematic illustration of an ultrasonic sensor [81]. (b) Photo of an ultrasonic sensor.

3.3. Sensor layouts

This paper reports laboratory tests carried out on three full-scale AAC members representative of the real bridge: two typical composite slab strips and one slab consisting of three slab strips. The slab strips are intended to evaluate their flexural and shear behaviour, respectively, while the slab is designed to investigate possible redistribution during flexural and shear failure in addition to validating the results of the slab strips. Because ultrasonic measurements are inherently local, with each actuator-receiver pair sampling only a limited volume of structure, the embedded sensors are placed selectively at critical cross sections corresponding to the expected flexural- and shear-critical regions. The full-scale tests are therefore designed to link the local ultrasonic response in these regions to the progressive deterioration of the overall structural behaviour. The full experimental program also includes experiments that investigate the long-term behaviour and fatigue behaviour of the system, further details are available in specific reports upon request.

The dimensions of the slab strips in the flexural test are detailed in Fig. 4, with a total length of 7350 mm. The precast beam is 300 mm in height, while the total height of the slab strip is 420 mm. Fifteen sensors, labelled BF1 (abbreviation of Beam Flexural sensor 1) to BF15 shown in Fig. 4(b), are strategically positioned. The bottom sensor row (BF1 to BF6) monitors flexural crack initiation. The middle row (BF7 to BF12) collaborates with the bottom row to monitor the propagation of flexural cracks at the mid-depth, while also working with the top row (BF13 to BF15) to monitor potential compression failure in the compression zone of the precast beam. Additionally, internal cracks may develop at the interface between cast-in-situ and precast beam without visible surface manifestations. However, this phenomenon was not observed in all members and is examined further in the Discussion. The details of the sensor locations are provided in Table 4. Fig. 5 shows a photo of installed sensors in the rebar cage before concrete casting. The sensors are fixed to the reinforcement cage and then fully embedded in the AAC when the beams are cast. There is no external coupling medium, and no repeated attachment or removal of the sensors during the tests. The mechanical coupling between sensor and concrete is therefore fixed once the concrete has hardened, which avoids variability due to changing contact pressure or re-positioning that is typical for surface-mounted transducers.

The composite beam designated for the shear test shares the same prestressing and dimensions as the flexural test beam, as depicted in Fig. 6. Sixteen sensors, labeled BS1 (abbreviation of Beam Shear sensor 1) to BS16, are strategically placed within the critical shear zone. The bottom row (BS1 to BS7) is dedicated to tracking the initiation of flexural cracks. This row also works in tandem with the middle row (BS8 to BS12) and the top row (BS13 to BS16) to detect collaboratively the initiation and propagation of shear cracks within the critical shear zone. The sensor locations are detailed in Table 5.

The AAC bridge slab comprises three precast beams, aligned with the dimensions of the beams used in the flexural and shear tests, as illustrated in Fig. 7. These beams are interconnected by cast-in-situ concrete and transverse reinforcement, maintaining a total height of 420 mm.

Table 4
Locations of sensors relative to the coordinate (coloured in red) in Fig. 4.

Sensor	BF1	BF2	BF3	BF4	BF5	BF6	BF7	BF8
x [mm]	3070	3315	3560	3815	4070	4325	3070	3315
y [mm]	77	77	77	77	77	77	277	277
z [mm]	550	550	550	550	550	550	550	550
Sensor	BF9	BF10	BF11	BF12	BF13	BF14	BF15	
x [mm]	3560	3815	4070	4325	3420	3665	3915	
y [mm]	277	277	277	277	360	360	360	
z [mm]	550	550	550	550	550	550	550	

Fig. 5. Photo of the installed sensors in the rebar cage before concrete casting.

Sensors are embedded in the middle composite beam, labeled SF1 (abbreviation of Slab Flexural sensor 1) to SF15, shown in Fig. 7(b), and the side composite beam, labeled SS1 (abbreviation of Slab Shear sensor 1) to SS13, shown in Fig. 7(c). Sensor functions mirror those described for the beams in the respective tests. The locations of sensors in the middle composite beam and the side composite beam are outlined in Tables 6 and 7, respectively.

4. Experimental setup and measurement plan

The flexural test setup for the AAC composite beam is depicted in Fig. 8, utilizing a four-point bending configuration with loading points spaced at 2400 mm. To capture the crack initiation and propagation,

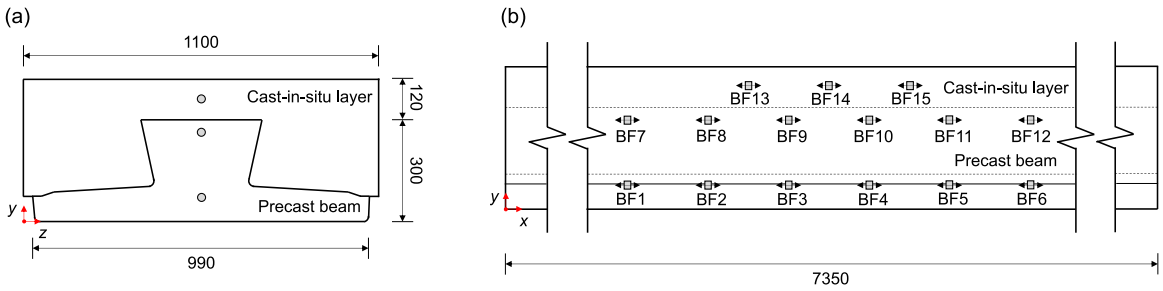

Fig. 4. Dimension of the AAC composite beam for the flexural test and its sensor layout (black arrow on the sensor indicates its polarization direction). The precise locations of the sensors are detailed in Table 4. (a) Cross-sectional view (unit: mm). (b) Front view (unit: mm).

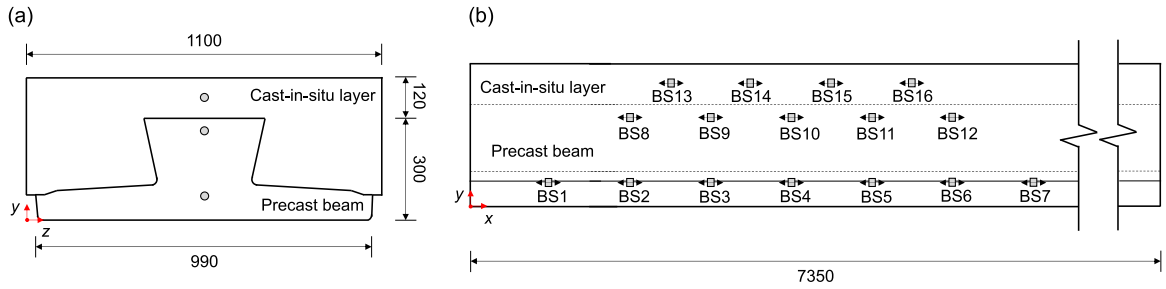

Fig. 6. Dimension of the AAC composite beam for the shear test and its sensor layout (black arrow on the sensor indicates its polarization direction). The precise locations of the sensors are detailed in Table 5. (a) Cross-sectional view (unit: mm). (b) Front view (unit: mm).

Table 5
Locations of sensors relative to the coordinate (coloured in red) in Fig. 6.

Sensor	BS1	BS2	BS3	BS4	BS5	BS6	BS7	BS8
x [mm]	260	505	760	1015	1270	1550	1810	505
y [mm]	77	77	77	77	77	77	77	277
z [mm]	550	550	550	550	550	550	550	550
Sensor	BS9	BS10	BS11	BS12	BS13	BS14	BS15	BS16
x [mm]	760	1015	1270	1550	640	880	1130	1380
y [mm]	277	277	277	277	340	345	345	350
z [mm]	550	550	550	550	550	550	550	550

two digital cameras are employed, one focusing on the side surface and the other on the bottom surface, for digital image correlation (DIC) measurements, as illustrated in Figs. 8(a) and 8(b). The camera coverage areas are also indicated in the figure. For tracking deformation and strain changes during the test, several LVDTs are strategically placed on the member. However, in this study, we specifically use one LVDT at the midspan, positioned as shown in Fig. 8, to assess the load-deflection curve at this critical location. A photo of the test setup can be found in Fig. 8(c). Further details on the experimental setup and structural performance can be found in our prior work [82,83].

The loading protocol for the flexural test is shown in Fig. 9. Note that the load levels in Fig. 9 represent the total load applied by both jacks. The ultrasonic measurements are conducted at specific loading steps, marked by red dots in Fig. 9. At each measurement point, data acquisition follows a round-robin approach: each sensor acts as the transmitter in turn, while the remaining sensors (excluding the active transmitter) function as receivers. The measurement sequence completes after *N* cycles (*N* is the number of sensors), ensuring every sensor serves as the transmitter exactly once. To achieve this, we developed a multi-channel multiplexer-based data acquisition (DAQ) system, which can automatically perform these acquisition tasks during signal recording [84]. The input electrical signal for sensor activation is a one-cycle squared pulse with a duration of 18.5 μs and an amplitude of

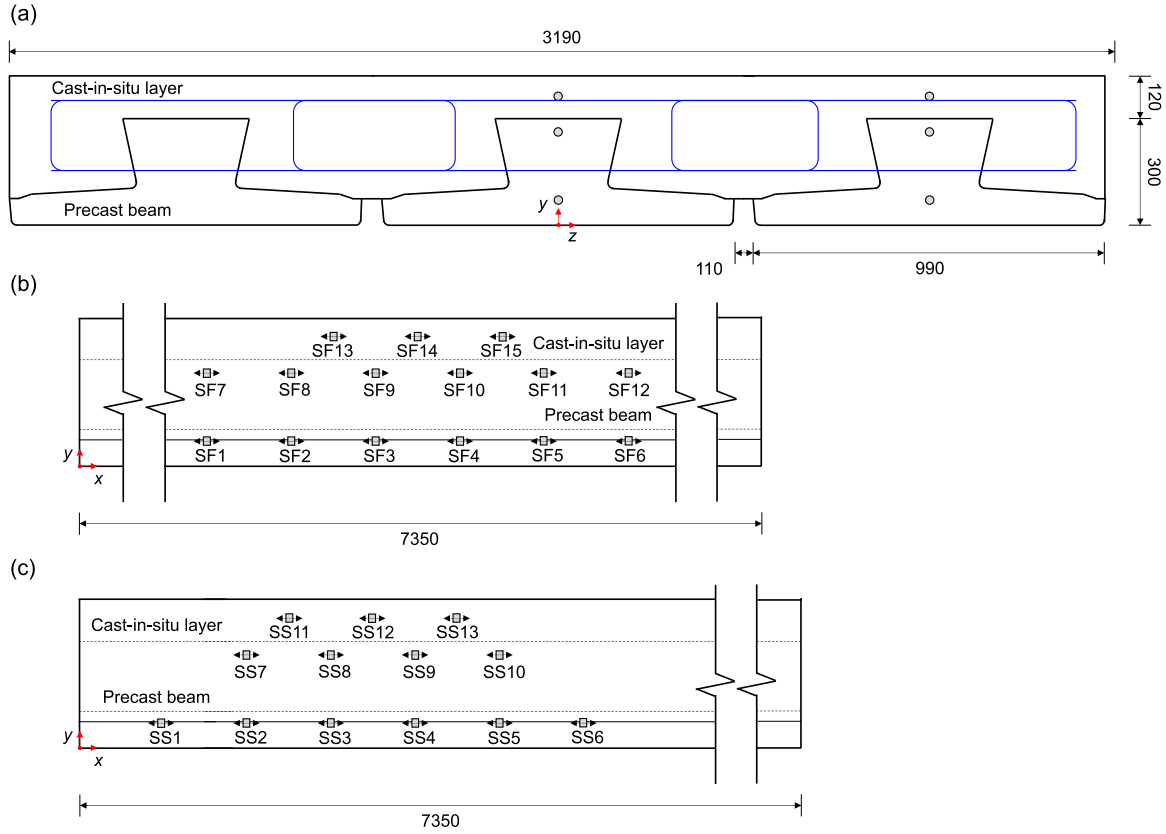

Fig. 7. Dimension of the AAC slab and the sensor layout (black arrow on the sensor indicates its polarization direction). (a) Cross-sectional view of the slab (unit: mm). Blue lines indicate the transverse reinforcements. (b) Front view of the middle beam (unit: mm). The precise locations of the sensors are detailed in Table 6. (c) Front view of the side beam (unit: mm). The precise locations of the sensors are detailed in Table 7.

Table 6
Locations of sensors in the middle beam relative to the coordinate (coloured in red) in Fig. 7(b).

Sensor	SF1	SF2	SF3	SF4	SF5	SF6	SF7	SF8
x [mm]	3030	3290	3550	3795	4050	4300	3030	3290
y [mm]	77	77	77	77	77	77	77	277
z [mm]	0	0	0	0	0	0	0	0
Sensor	SF9	SF10	SF11	SF12	SF13	SF14	SF15	
x [mm]	3550	3795	4050	4300	3420	3680	3925	
y [mm]	277	277	277	277	340	340	340	
z [mm]	0	0	0	0	0	0	0	

Table 7
Locations of sensors in the side beam relative to the coordinate (coloured in red) in Fig. 7(c).

Sensor	SS1	SS2	SS3	SS4	SS5	SS6	SS7
x [mm]	275	535	795	1015	1265	1535	535
y [mm]	77	77	77	77	77	77	277
z [mm]	1100	1100	1100	1100	1100	1100	1100
Sensor	SS8	SS9	SS10	SS11	SS12	SS13	
x [mm]	795	1015	1265	690	945	1185	
y [mm]	277	277	277	340	345	345	
z [mm]	1100	1100	1100	1100	1100	1100	

200 V. The sampling rate is 3 MHz, and the maximum duration of the recorded signal is 3000 μs (9000 samples). Random noise is reduced using a stacking process, in which 5 repeated signals are averaged.

The shear test configuration for the composite beam is shown in Fig. 10, with the loading point situated 1200 mm away from the support. Aligning with the approach employed in the flexural test, we incorporated two digital cameras for DIC measurements, one dedicated to the side surface and the other to the bottom surface, as also depicted in Figs. 10(a) and 10(b). Additionally, a vertical LVDT placed beneath the loading point is used to track the load-deflection curve at this critical location, and its placement is indicated in Fig. 10. A photo of the test setup is shown in Fig. 10(c). The shear test loading protocol is illustrated in Fig. 11, with red dots marking the load levels where ultrasonic measurements were taken. Each measurement adhered to the same data acquisition method described earlier.

For the slab flexural test, the loading point is positioned at the midspan of the middle beam, as shown in Fig. 12. A single camera is deployed to cover the area of the bottom surface under the loading point. A vertical LVDT is used to track the deflection at the midspan, as also indicated in Fig. 12(a). It should be noted that the type of support used in the slab test differs from that in the beam tests. The beam tests utilize hinge and roller supports, whereas the slab tests employ elastomeric supports. A photo of the test setup can be found in Fig. 12(b). The loading protocol for the slab flexural test is illustrated in Fig. 13, with red dots marking the load levels where ultrasonic measurements were taken. Each measurement adhered to the same data acquisition method described earlier.

The slab shear test is conducted on the same slab for the flexural test but performed nine days later. The load is applied 1200 mm away from the support, with the loading point situated between the middle beam and the side beam, as depicted in Fig. 14. To capture the cracking behaviour beneath this loading point, a digital camera was positioned to cover the corresponding area. The deflection of the side beam containing sensors was measured through a vertical LVDT, whose placement is also indicated in Fig. 14(a). A photo of the test setup is shown in Fig. 14(b). The loading protocol for the slab shear test is illustrated in Fig. 15, with red dots marking the load levels where ultrasonic measurements were taken. Each measurement adhered to the same data acquisition method described earlier.

5. Validation of damage indicators

5.1. Time-domain signal analysis and parameter selection for damage indicators

Before proceeding with the signal processing for DIs, we first check the received waveforms. Fig. 16 shows the time-domain responses of the measured signals under varying applied loads in the beam for the shear test. Raw signals are used without any pre-processing or filtering. In Figs. 16(a) and 16(c), the complete waveforms are presented over a time interval of 0–3000 μs received by the sensor pairs BS2-BS3 and BS8-BS3, where the initial sensor number indicates the actuator. Discernible variations in amplitude can be observed as the applied load increases. Additionally, the signal amplitude for the sensor pair BS2-BS3 at 390 kN remains relatively high, while that for the sensor pair BS8-BS3 at the same load level decreases dramatically. To facilitate a more detailed comparison, Figs. 16(b) and 16(d) provide magnified views of a selected time window with a length of 100 μs. These enlarged figures indicate that the differences in amplitude, phase shift, and waveform become more pronounced with the increasing load. Additionally, the phase delay of the signal collected from the sensor pair BS8-BS3 is more significant than that collected from the sensor pair BS2-BS3. Collectively, these results demonstrate that applied mechanical loading exerts a significant influence on the temporal features of the propagating signals. Furthermore, the signal responses collected from different sensor pairs exhibit different signal characteristics.

As mentioned in Section 2.2, given the subtle nature of crack initiation in concrete, we use the *CC* value, computed with the wave interferometry technique, as a metric for data analysis. In the context of detecting the crack initiation, the primary emphasis is on identifying this initiation within the prestressed beam of the bridge. This beam serves as the primary load-bearing component critical to the structural integrity of the entire system. Therefore, it is crucial to note that, in this section on the initial crack detection, only the sensors placed in the prestressed beams are used.

When applying the DWI technique, two key aspects were considered: (1) the time window should be sufficiently long to ensure that the wave propagation envelope samples the bottom surface of the beam, where flexural cracks initiate; (2) since ultrasonic measurements were conducted only at discrete load steps rather than continuously, the similarity between successive waveforms should remain high in order to maximize sensitivity to the onset of cracking. Based on the first aspect, we select a time window beginning at the first arrival with a duration of 100 μs, which is expected to contain sufficient P-wave energy. This window contains at least five oscillation cycles, as shown in Figs. 16(b) and 16(d), which ensures statistical robustness for correlation analysis [85]. For two adjacent sensors along the bottom row, since the selected 100 μs window starts at the first arrival, roughly 50 μs, the latest arrivals included are around 150 μs, corresponding to a maximum propagation distance of ~600 mm (estimated by assuming a P-wave velocity of 4000 m/s), which is much larger than the reflected wave path from the bottom surface of around 294 mm (calculated using a sensor distance of 250 mm and the distance from the sensor to the bottom surface of 77 mm). Hence, the wavefield within this time window is expected to sample the bottom surface region where cracks initiate. Regarding the second aspect, we employ a stepwise reference approach, where each signal is compared with that from the previous load step, to stabilize the *CC* across discrete load steps and enhance sensitivity to cracking. Furthermore, using a longer time window would integrate more incoherent wave components, thus reducing the *CC* even in the absence of cracking and lowering its sensitivity to initial crack formation. For these reasons, the 100 μs window provides a balanced choice between geometric coverage and sensitivity for crack detection.

Fig. 17 illustrates the different behaviours of velocity change retrieved using DWI for sensor pairs in the tension and compression zones of the beam during the flexural test under increasing load. For the

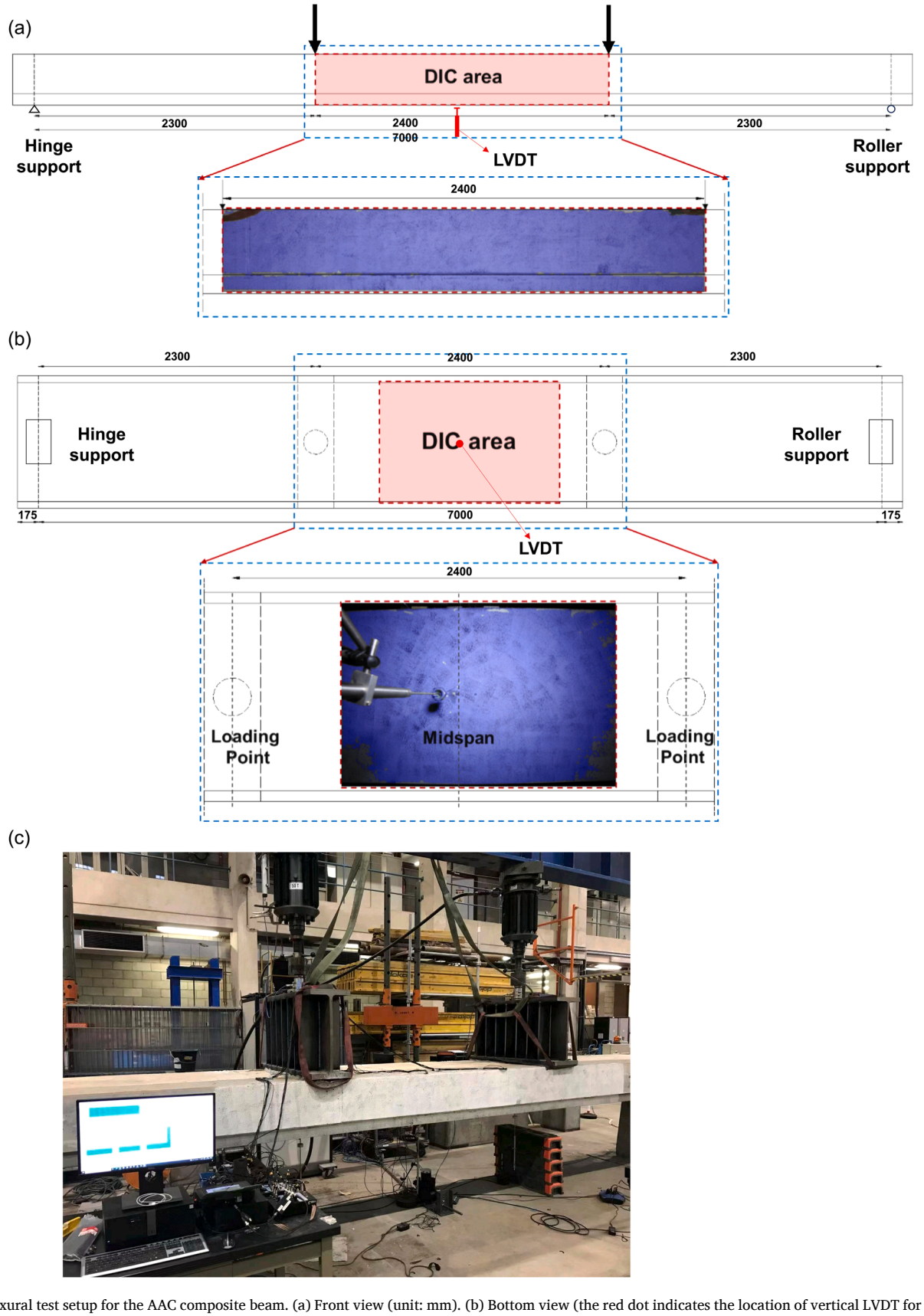

Fig. 8. Flexural test setup for the AAC composite beam. (a) Front view (unit: mm). (b) Bottom view (the red dot indicates the location of vertical LVDT for measuring deflection; unit: mm). (c) Photo of the test setup.

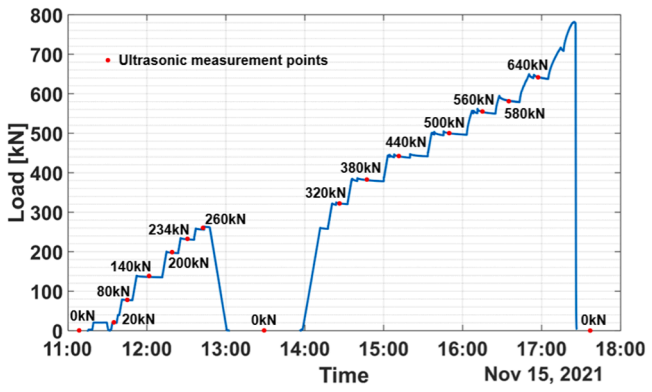

Fig. 9. Measuring points for the flexural test of the AAC composite beam (total load of two jacks).

sensor pair BF1-BF2 in the tension zone shown in Fig. 17(a), stepwise DWI results show that the differential velocity change remains relatively stable at lower loads, but a sudden jump occurs around 380 kN, accompanied by a *CC* below 0.5. The apparent magnitude of this velocity change exceeds 50‰, which is orders of magnitude larger than can be explained by the acoustoelastic effect in concrete (typically below 2‰/MPa [86–88]). This unrealistic result indicates an artefact caused by cycle skipping, where the correlation procedure mistakenly aligns with an adjacent oscillation cycle [89]. Because cycle skipping can seriously compromise the reliability of DWI and mislead physical interpretation, the UPV technique is used to more robustly track crack propagation.

Furthermore, two drops in *CC* are observed before 400 kN: one at 260 kN and another at 380 kN. At 260 kN, no significant velocity change is detected, and the negative shift may reflect the combined influence of tensile stress and microcracking, making it difficult to draw firm conclusions. In contrast, *CC* is more directly related to structural changes in the medium, and previous studies have shown that a significant *CC* reduction is strongly associated with cracking in concrete [50]. This motivates the use of *CC* as the primary indicator for initial cracking.

Fig. 17(b) shows the accumulated velocity change and *CC* from sensor pairs in the compression zone (BF9-BF8 and BF9-BF10) and tensile zone (BF3-BF2 and BF3-BF4). Since ultrasonic measurements in both the compression and tension zones were performed under identical experimental conditions using the same instrumentation, noise-, instrumentation-, and environment-induced variations in the accumulated velocity change and *CC* can be considered comparable in the two zones and are therefore excluded as the primary cause of the observed differences. The *CC* in the compression zone remains close to 1, with only minor fluctuations. This suggests that the stress and environmental variations during testing produce only small changes in *CC*. Consequently, the pronounced *CC* reduction observed in the tension zone cannot be attributed to stress or environmental effects alone.

The increase in accumulated velocity change is consistent with the acoustoelastic effect [90–92], where wave velocity increases linearly with increasing compressive stress. Strictly speaking, the observed response reflects a coupled effect of stress and temperature variations. Given that the test was conducted in the laboratory over only a few hours and that the accumulated velocity change varies almost linearly with the applied load, stress-induced effects are likely to account for the larger portion of the measured velocity changes. To relate these observations to stress-induced effects, we carried out a simplified sectional analysis at the load level of 380 kN. Assuming a rectangular cross section ($1100 \times 420\ mm^2$) and a neutral axis at mid-depth of the section, the tensile and compressive stresses at the sensor locations in the tensile and compression zones are about $+8.6$ MPa and -4.3 MPa, respectively. The tensile-zone stress amplitude is therefore roughly twice that in the compression zone. Using the measured velocity changes in the compression zone together with these stresses, we estimate an effective acoustoelastic parameter of about 1.3 $(GPa)^{-1}$ for the geopolymer concrete, i.e. a change of 1 MPa in stress leads to an order of 1.3‰ change in wave velocity. This value is consistent with the order of magnitude reported in the literature for concrete [43,54,86,87,93]. Even allowing for mechanical response differences between tension and compression, a factor of two in stress amplitude cannot reasonably account for the approximately sevenfold difference in velocity-change magnitude between the tensile and compression paths. We therefore conclude that the velocity changes in the tensile zone are dominated by the combined effect of stress and cracking, with cracking playing the leading role. This also supports our original choice not to use velocity change as an indicator of crack initiation in Section 2.1.

For robustness against non-structural changes (i.e., spatial fluctuations of mechanical properties [47]) in the concrete, the proposed DI employs relative wave velocity calculated using UPV, which is relative to the wave velocity at 0 kN before the test. Unlike DWI, UPV does not require a stepwise reference because it relies solely on the arrival time of the direct wave, which can be identified even when overall waveform similarity is low.

5.2. DI for crack initiation

The *CC* values at various load levels (140 kN, 200 kN, and 260 kN) for the flexural test beam are depicted in Fig. 18. Prior to reaching 140 kN, there is no significant change in *CC* values, suggesting the absence of visible cracks. However, at 200 kN, a noticeable drop in *CC* values occurs at specific sensor pairs (BF2-BF3, BF3-BF4 and BF5-BF6), registering values below 0.85, as shown in Fig. 18(d). This decline indicates changes in the structure between 140 kN and 200 kN. The reduction in the waveform coherency is strongly influenced by the structural changes in the medium [94], reinforcing the likelihood that these *CC* drops are linked to concrete cracking. Additionally, the magnitude of *CC* reduction also aligns with the observation of crack-induced *CC* reduction from the literature [48,50,51], where similar magnitude of *CC* reduction, around 0.15, and crack initiation were observed simultaneously.

To validate the possible crack initiation in the beam, we cross-referenced the ultrasonic results with the DIC measurements on the bottom surface of the beam midspan, as illustrated in Fig. 19. At 140 kN, no cracks are evident in the DIC measurement. However, upon reaching 200 kN, the DIC measurement confirmed the presence of a crack between BF3 and BF4, aligning with the ultrasonic findings. Notably, it is difficult to observe cracks in the sensor pairs BF2-BF3 and BF5-BF6. The former sensor pair is obstructed by the vertical LVDT at midspan, while the latter is affected by high noise levels in that region due to out-of-plane motions [95]. Since this bending-induced out-of-plane motion is non-rigid, current compensation methods (e.g., the one proposed by Pan et al. [96]) cannot resolve the issue. Out-of-plane motions may introduce spurious strain fluctuations, which may further reduce the sensitivity of DIC to detect small strain localizations associated with early crack initiation. As a result, the strain patterns in the outer zones are dominated by noise and less informative for crack identification. Nevertheless, the strain localization patterns in the central region remain consistent with the test image, confirming the robustness of the DIC result in this region, as shown in Fig. 19(c). Therefore, although the outer areas are influenced by noise and less sensitive to crack initiation, DIC images, especially their central region, provide meaningful information regarding crack patterns. At higher load levels of 260 kN, as shown in Fig. 18(c), more trajectories within the sensor network exhibit low *CC* values, signifying the presence of multiple cracks. This observation is corroborated by the DIC measurement at this load level, as illustrated in Fig. 19(c). In Fig. 18(d), we examined alternative *CC* thresholds of 0.90 and 0.80. Using $CC = 0.90$ causes the onset flag to appear at relatively low loads (for some paths around 140 kN), i.e., ahead of any cracking indicated by DIC. In contrast, adopting $CC = 0.80$

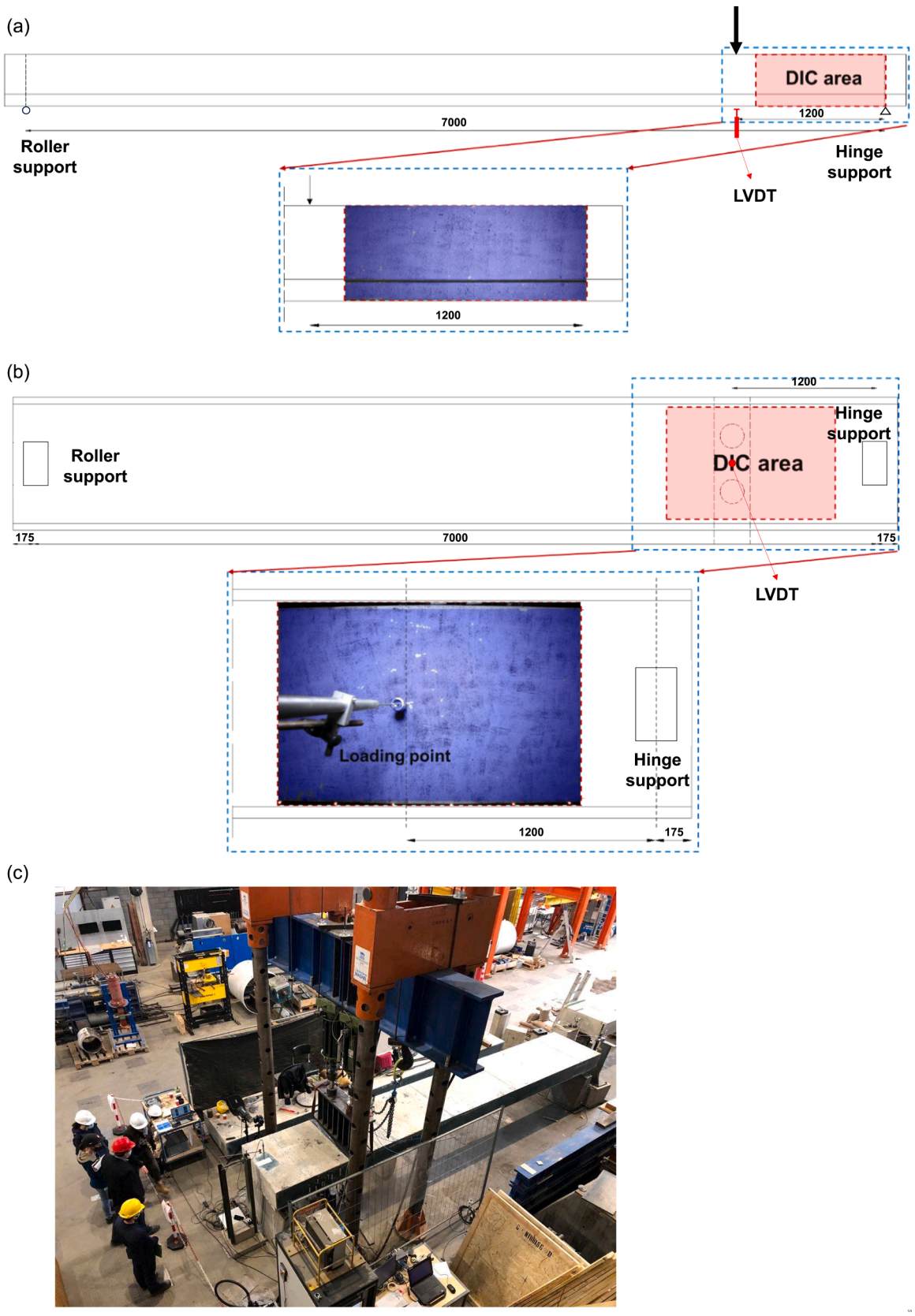

Fig. 10. Shear test setup for the AAC composite beam. (a) Front view (unit: mm). (b) Bottom view (the red dot indicates the location of vertical LVDT for measuring deflection; unit: mm). (c) Photo of the test setup.

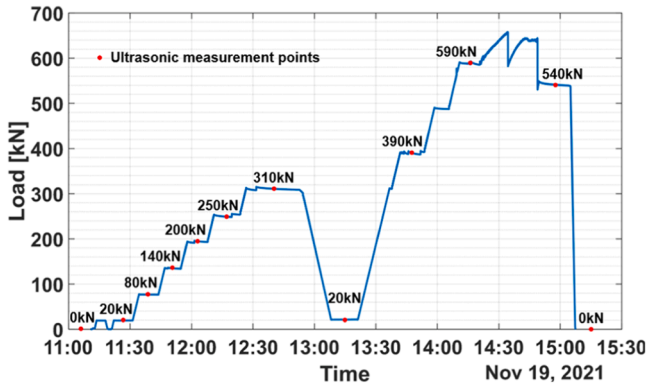

Fig. 11. Measuring points for the shear test of the AAC composite beam.

shifts the first threshold crossing to later load steps, when cracking is already apparent in DIC. Hence, neither extreme provides a robust crack-initiation criterion for the beam flexural test.

For the shear test beam, the *CC* values at various load levels (250 kN and 310 kN) are shown in Fig. 20. A drop in *CC* value is observed between 250 kN and 310 kN. Similar to the flexural test of the beam, a *CC* value below 0.85 corresponds to this change, as shown in Fig. 20(c). It is crucial to note that, despite this observation, direct validation using the DIC technique faces challenges. In Fig. 21, we present DIC measurements from the bottom surface of the beam at 310 kN. Although the outer regions again exhibit substantial noise due to out-of-plane motions, a consistent strain localization pattern is still visible (Figs. 21(a) and 20(b)), confirming that the DIC results remain reliable. For Fig. 20(c), we repeated the check with $CC = 0.90$ and 0.80. The 0.90 threshold proves overly sensitive and tends to declare crack initiation earlier than supported by the DIC observations. Lowering the threshold to 0.80 produces crack-onset loads that are generally close to those obtained with 0.85, although a few sensor paths show noticeable differences in the trigger point. Given the need for a single, comparable criterion across members, we maintain $CC = 0.85$ as a pragmatic compromise that limits premature triggering while preserving sensitivity to the first cracking stage.

In the flexural test of the slab, a notable decrease in *CC* values is observed between 280 kN and 400 kN, as illustrated in Fig. 22. Specifically, *CC* values along suspicious trajectories fell below 0.85, as shown in Fig. 22(c), aligning with the previous observations of crack initiation. The DIC measurements at 280 kN and 400 kN are presented in Fig. 23. Despite the constrained observable area, a discernible crack is still evident between the sensor pair SF1-SF2. Since the shear test of the slab was conducted later than the flexural test with cracks already initiated in the structure, we do not discuss the crack initiation in the shear test of the slab. Threshold sensitivity was also evaluated in Fig. 22(c) by comparing the value 0.85 with 0.90 and 0.80. With $CC = 0.90$, several paths remain above the threshold throughout the test, so crack initiation would not be detected at the load step where DIC first identifies cracking. With $CC = 0.80$, early cracking can be missed on specific paths (e.g., SF1-SF2) or detected only after the DIC-observed onset. Considering these outcomes together with the beam and slab results, $CC = 0.85$ provides the most consistent match to the DIC-based crack-initiation stage across the tested specimens and is therefore adopted in this study.

5.3. DI for crack propagation

To monitor the behaviour of prestressed beams and the cast-in-situ layer in the loading process, we extend our analysis to include sensors embedded both in the beam and the cast-in-situ layer. In Fig. 24(a), the relative velocity is depicted at the load level (200 kN), where crack initiation is observed during the flexural test on the beam. Notably, there is no conspicuous change in relative velocity. This is because the calculation of *CC* employs the waveform within a certain time window, whose wave paths sample a larger region. Consequently, *CC* is particularly sensitive to potential cracks within this region. In contrast, the wave trajectory of ballistic velocity is a straight line between the transmitter and receiver, making it sensitive only to major cracks that cause significant delays due to possible alternations in the wave path. Given that cracks in the flexural test initiate on the bottom surface where the trajectories of the first arrival waves cannot extend, these initial cracks have very limited impact on the relative velocity derived using the UPV technique.

Between load levels of 200 kN and 320 kN, cracks develop gradually, and no significant change in relative velocity is apparent (see Fig. 24(b)). At a load level of 380 kN, the relative velocity of the sensor pair BF1-BF2 experiences a sudden and substantial decrease, falling below 0.9, as shown in Fig. 24(c). The observed velocity change, more than 10%, cannot be explained by the stress change in the beam, which typically induces velocity changes on the order of 1‰ [54]. The only plausible explanation for this reduction is the development of cracks along the wave trajectory, which causes significant delay due to potential alterations in the wave path. Consequently, this magnitude of the relative velocity reduction is attributed to cracking. Fig. 24(d) shows the relative velocity vs. applied load for selected sensor pairs on the bottom row. After reaching 380 kN, the relative velocity of these sensor pairs continues to reduce, and the relative velocities of all selected sensor pairs are below 0.9 at 500 kN.

Additionally, as explained in Section 2.3, when the propagation direction of elastic waves is perpendicular to the crack orientation, the travel time increases significantly, leading to a consequential decrease in velocity. Considering that cracks in the flexural test initiate at the bottom fibre and propagate upward during loading, the observed cracks at the locations of two sensor pairs are likely the result of propagated flexural cracks. Notably, given that the bottom row of sensors is positioned higher than the centroid of prestressing strands, cracks reaching the sensor network suggest a probable extension to the strands as well. At the same load level, substantial cracks can be observed in the bottom DIC measurement, as shown in Fig. 25. Additionally, after reaching the 380 kN load level, the load-deflection curve shown in Fig. 26 immediately manifests strong nonlinearity, signifying the presence of residual deformation in the member. At 500 kN, where the relative velocities of all sensor pairs on the bottom sensor row are below 0.9, the whole structure exhibits obvious nonlinearity in the load-deflection curve. Given the limitations of the DIC technique in capturing crack propagation inside concrete structures, the use of embedded sensors enables exploration of the internal damage of the structure, providing insights into the processes that the DIC technique may not effectively capture.

In the shear test of the beam, crack initiation occurs at 310 kN. Fig. 27(a) illustrates that, at this load level, there are no significantly low values in the relative velocity within the sensor network. However, at the next load level of 390 kN, specific sensor pairs between the top and bottom rows of sensors exhibit a relative velocity lower than 0.9, while others maintain relatively high levels, as shown in Fig. 27(b). In Fig. 27(c), we present the relative velocities for the selected inclined sensor pairs (BS8-BS3, BS8-BS4, BS8-BS5, BS8-BS6, BS8-BS7). At 390 kN, three trajectories have relative velocity lower than 0.9, while all these selected trajectories show low relative velocities after this load level. These low relative velocities are most likely attributed to cracking.

As mentioned in Section 2.3, ballistic wave velocity is sensitive to cracks oriented perpendicular to wave propagation. The relative velocities depicted in Fig. 27(b) suggest that the orientation of cracks is from the origin to the loading point, characteristic of diagonal cracks in the shear-critical zone, which are identified as shear cracks. These cracks, occurring inside the prestressed beam covered by a cast-in-situ layer, remain undetected by surface measurements such as DIC measurements. Fig. 28 presents the DIC measurements at 390 kN, revealing no observable evidence of shear cracks in the beam. Similar to the observation in the flexural test of the beam, strong nonlinearity in the load-

(a)

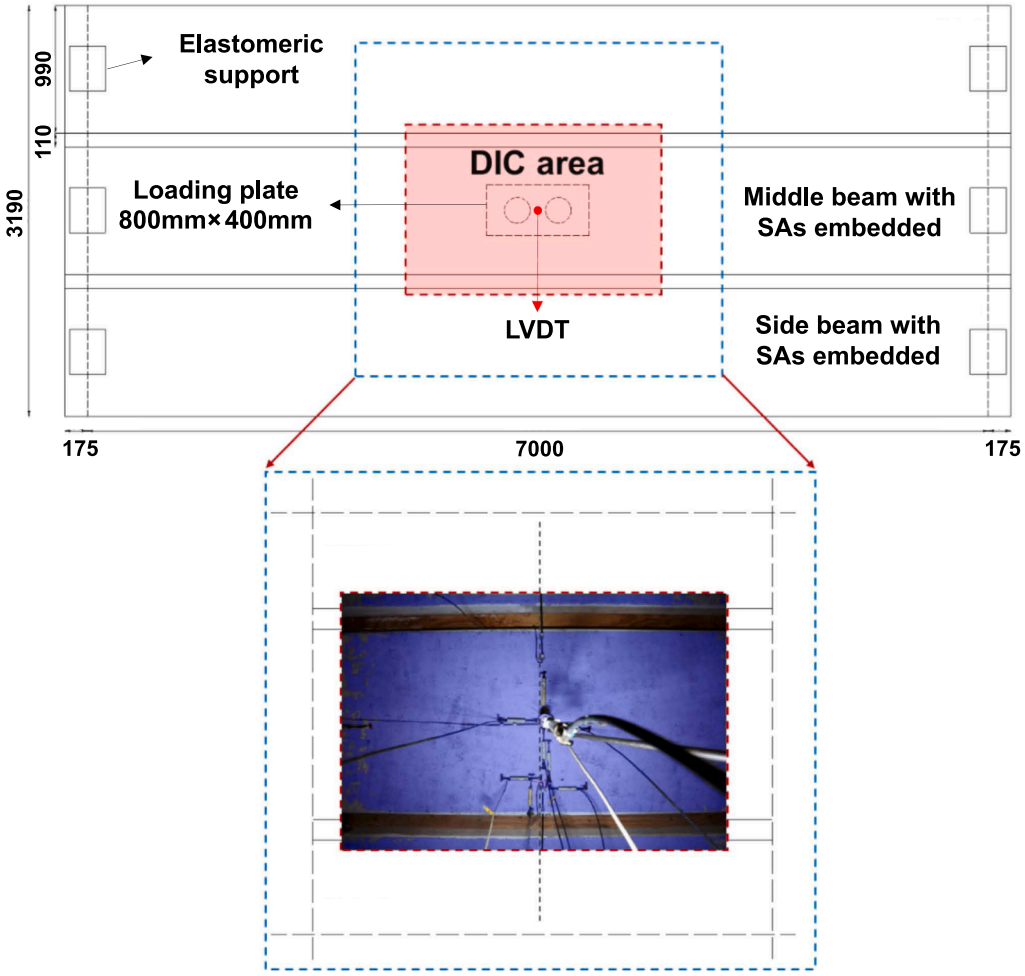

(b)

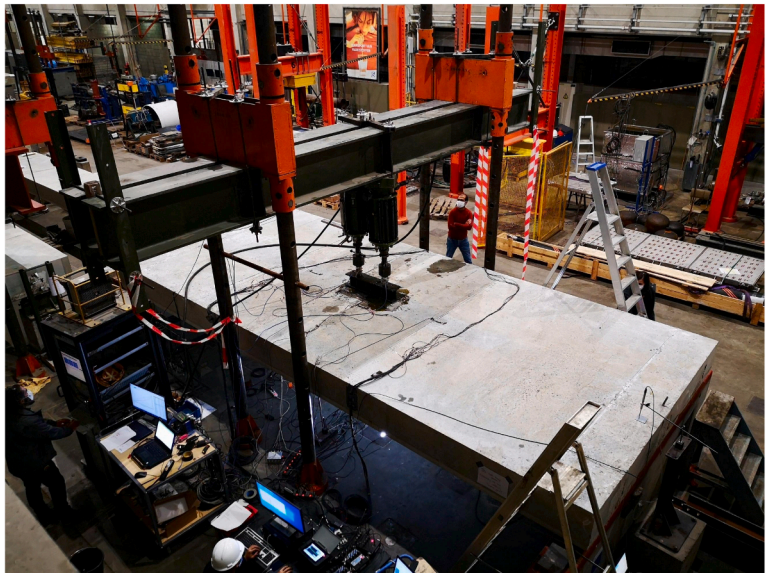

Fig. 12. Flexural test setup for the solid slab. (a) Bottom view (the red dot indicates the location of vertical LVDT for measuring deflection; unit: mm). (b) Photo of the test setup.

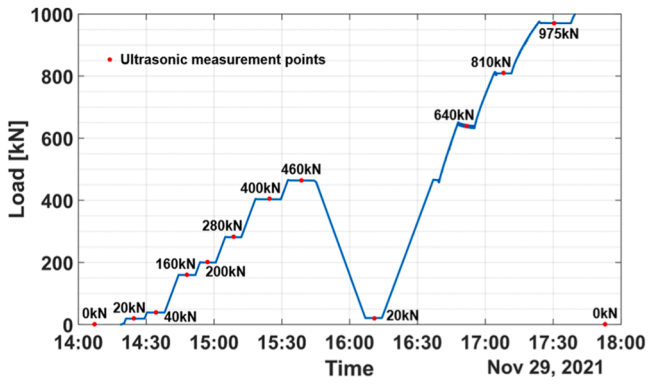

Fig. 13. Measuring points for the flexural test of the solid slab.

deflection curve is observed beneath the loading position immediately after the observation of diagonal cracks, as illustrated in Fig. 29.

Similar behaviour is observed in the slab tests. In the flexural test on the slab, relative velocities for nearly all sensor pairs on the bottom row at 810 kN fall around or below 0.9, as illustrated in Fig. 30. Concurrently, a subtle nonlinearity in the load-deflection curve at midspan becomes apparent, as highlighted in Fig. 31. For the shear test of the slab, this drop is observed at 760 kN (refer to Fig. 32). Additionally, the propagation of diagonal cracks is clearly shown in Fig. 32(b), where the relative velocity decreases progressively along the ordered sensor pairs (SS7-SF3, SS7-SF4, SS7-SF5). Upon examining the load-deflection curve from the LVDT beneath the loading point, the structure demonstrates slightly nonlinear behaviour beyond this load level, as illustrated in Fig. 33.

6. Discussion

6.1. Possible delamination at the interface between cast-in-situ layer and precast beam

In Section 3.3, we noted our intention to use the middle row together with the top row to monitor potential compression failure in the compression zone or delamination between the precast beam and the cast-in-situ layer. However, a low relative velocity in this region was observed only in the beam subjected to the shear test, as shown in Fig. 34. Consistent with the observation in Fig. 27(b), only the trajectories running from top left to bottom right exhibited low relative velocities. As discussed in Section 5.3, this trajectory pattern indicated that the crack in this region was most likely a diagonal crack rather than delamination. If delamination had occurred, all trajectories would have exhibited low relative velocities. Because this finding is limited to a single member (the shear-test beam), it did not allow us to draw a generalized conclusion regarding the interface performance between the precast beam and cast-in-situ layer. Nonetheless, the observation in Fig. 34 highlights the potential risk of hidden damage in this region, which may not produce visible surface signs. Embedded ultrasonic sensors offer a promising solution for monitoring such damage. Future work should therefore explore more systematic monitoring strategies to cross-validate ultrasonic findings. In particular, ultrasonic pulse echo tomography [97] and embedded distributed fibre optic sensors [22] installed along the interface could complement ultrasonic sensors, to validate the detection and assessment of internal cracks.

6.2. Dispersion of elastic wave caused by the interaction between elastic waves and cracks

In this study, we deliberately focused on wave velocity as the primary indicator, since our objective was to propose a metric that could be applied robustly and reliably in practical structural monitoring scenarios. Although dispersion analysis is valuable for revealing additional information such as crack size and aperture, it is more sensitive to noise and generally increases implementation complexity. Therefore, this analysis was not considered in this study.

Nevertheless, in future work, we plan to investigate the dispersion of body waves in cracked concrete, with the aim of estimating crack width from travel-time changes across different frequency ranges. A possible approach will be to use the wavelet cross-spectrum (WCS) [98] to evaluate frequency-dependent travel-time changes and relate them to crack size. Two issues, however, will require careful consideration:

- The measured frequency-dependent travel-time change is a coupled effect, reflecting both fracture-induced and stress-induced contributions, as observed in our previous study [54]. To isolate the fracture-induced effect, it will be necessary to first quantify the magnitude of each contribution and then decouple them.
- When the medium is heavily cracked, the WCS technique may become less effective, since the similarity between two waveforms can be low and the phase change may be restricted to the range -π to π. In such cases, phase unwrapping may be required to reconstruct the true travel-time change [98].

6.3. Suggestions for the in-situ applications on concrete bridges

The threshold values of the DIs used in this study correspond to different limit states of the structure. Specifically, the value of 0.85 for CC is associated with the SLS, indicating the onset of serviceability-related crack initiation in the prestressed member. The value of 0.9 for relative velocity is related to the ULS, representing a condition where irreversible signs of structural damage may occur. These thresholds were established for a specific high-performance AAC system under controlled load-holding laboratory conditions and, therefore, cannot be directly applied to actual in-situ bridge behaviour, where traffic loads are transient. They should be regarded as indicative reference values for the AAC mixtures and structural configuration investigated here, rather than universal values for all AAC or ordinary concrete.

For long-term monitoring of concrete bridges using embedded sensors, signals can in principle be acquired periodically in an active transmitter-receiver mode to track the evolution of the structural condition over time. In this sense, the proposed DIs are intended to support lifetime monitoring, because they provide local ultrasonic features that are sensitive to crack-related changes. However, under real long-term service conditions, the interpretation of these DIs is not yet straightforward, since the measured responses may reflect the coupled influence of transient traffic-induced stress fluctuations, crack opening and closure under moving loads, shrinkage and creep, environmental variations, and possible long-term drift of the sensing system. Consequently, changes in *CC* and relative wave velocity cannot yet be uniquely attributed to a specific damage state without additional contextual information and decoupling procedures. For example, the long-term monitoring projects reported in the literature using embedded sensors mainly focus on tracking environment-induced changes [99,100] rather than directly assessing the structural state. In particular, the definition of a long-term baseline cannot at present be reduced to a single fixed reference state, because the reference response itself may evolve under these coupled environmental, operational, and material-aging effects. Therefore, the present study should be understood as a first step towards lifetime monitoring: it establishes and validates damage-sensitive ultrasonic features under controlled conditions, while further research is needed to develop multi-factor decoupling and adaptive baseline updating strategies for robust in-service interpretation. As a near-term and more interpretable application route, the proposed DIs may also be combined with proof load testing [101–103], where the loading history is known and the ambiguity of DI interpretation can be substantially reduced.

In this context, the relative wave velocity should not be interpreted

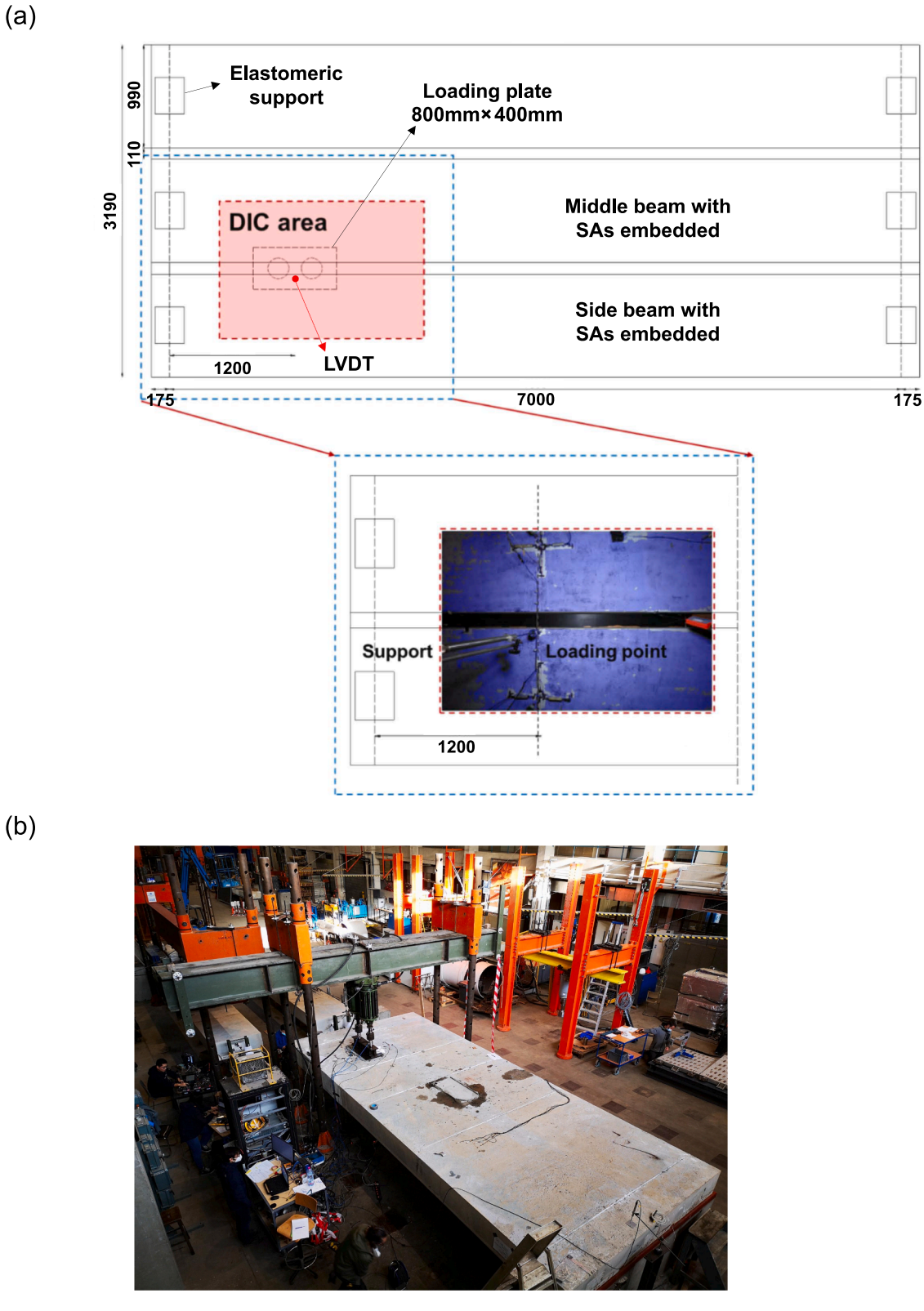

Fig. 14. Shear test setup for the solid slab. (a) Bottom view (the red dot indicates the location of vertical LVDT for measuring deflection; unit: mm). (b) Photo of the test setup.

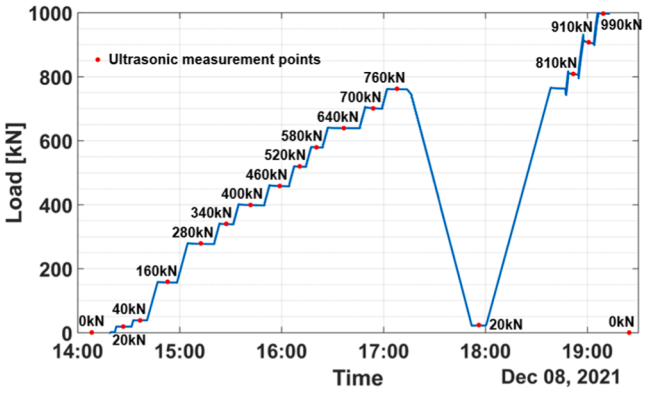

Fig. 15. Measuring points for the shear test of the solid slab.

as a direct quantitative measure of residual load-carrying capacity, nor as a standalone parameter capable of resolving all stages of crack development under normal service conditions. Rather, within the present framework, it should be regarded as a warning-oriented indicator whose interpretation becomes more meaningful when combined with complementary information on crack reopening/propagation, structural nonlinearity, stiffness degradation, and the loading and environmental context. Under unconstrained long-term in-service conditions, such interpretation will require further development of decoupling strategies to separate damage-related changes from other coupled influences. Controlled proof-loading scenarios provide an important intermediate application case, because the load history is known and the reopening of existing cracks can be intentionally promoted, thereby allowing the significance of relative wave velocity changes to be interpreted with reduced ambiguity.

As a near-term practical application route, proof load testing may be used to evaluate the proposed DIs under controlled boundary conditions.

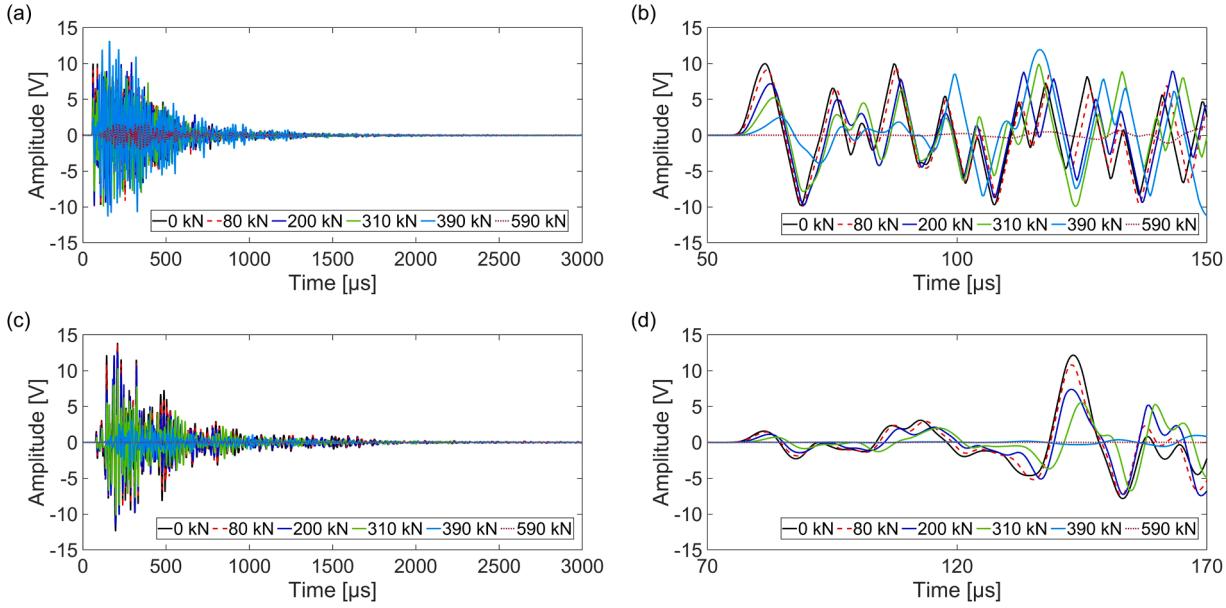

Fig. 16. Selected received signals in the beam for the shear test. (a) Signals collected from sensor pair BS2-BS3 at different load levels. (b) Magnified views of signals collected from sensor pair BS2-BS3 in the time window from 50 μs to 150 μs. (c) Signals collected from sensor pair BS8-BS3 at different load levels. (d) Magnified views of signals collected from sensor pair BS8-BS3 in the time window from 70 μs to 170 μs.

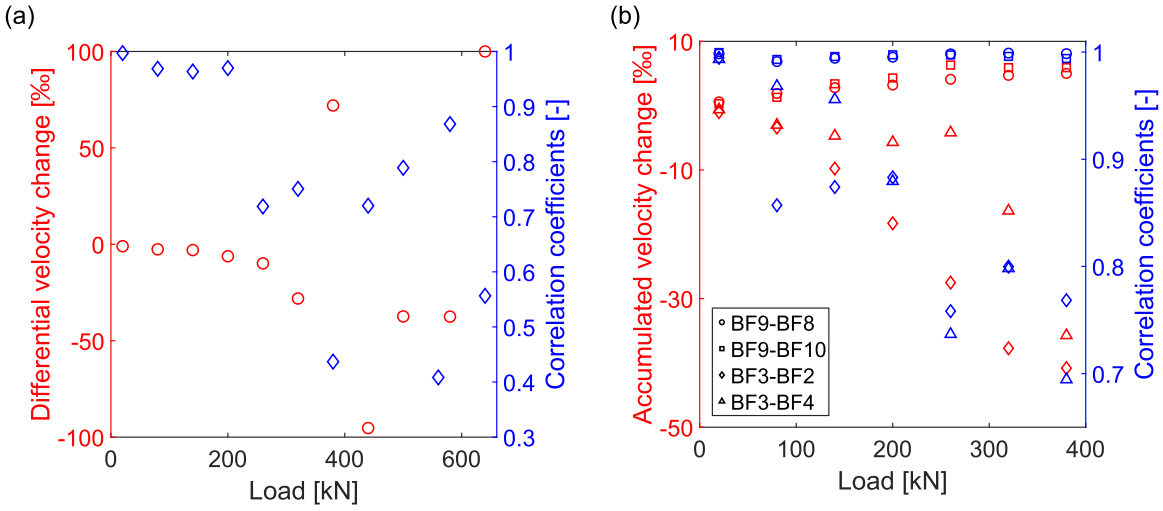

Fig. 17. Velocity changes and *CC* calculated using the stretching technique for selected sensor pairs. (a) Differential velocity change and *CC* from sensor pair BF1-BF2. (b) Accumulated velocity change and *CC* from sensor pairs in the compression zone (BF9-BF8 and BF9-BF10) and tensile zone (BF3-BF2 and BF3-BF4).

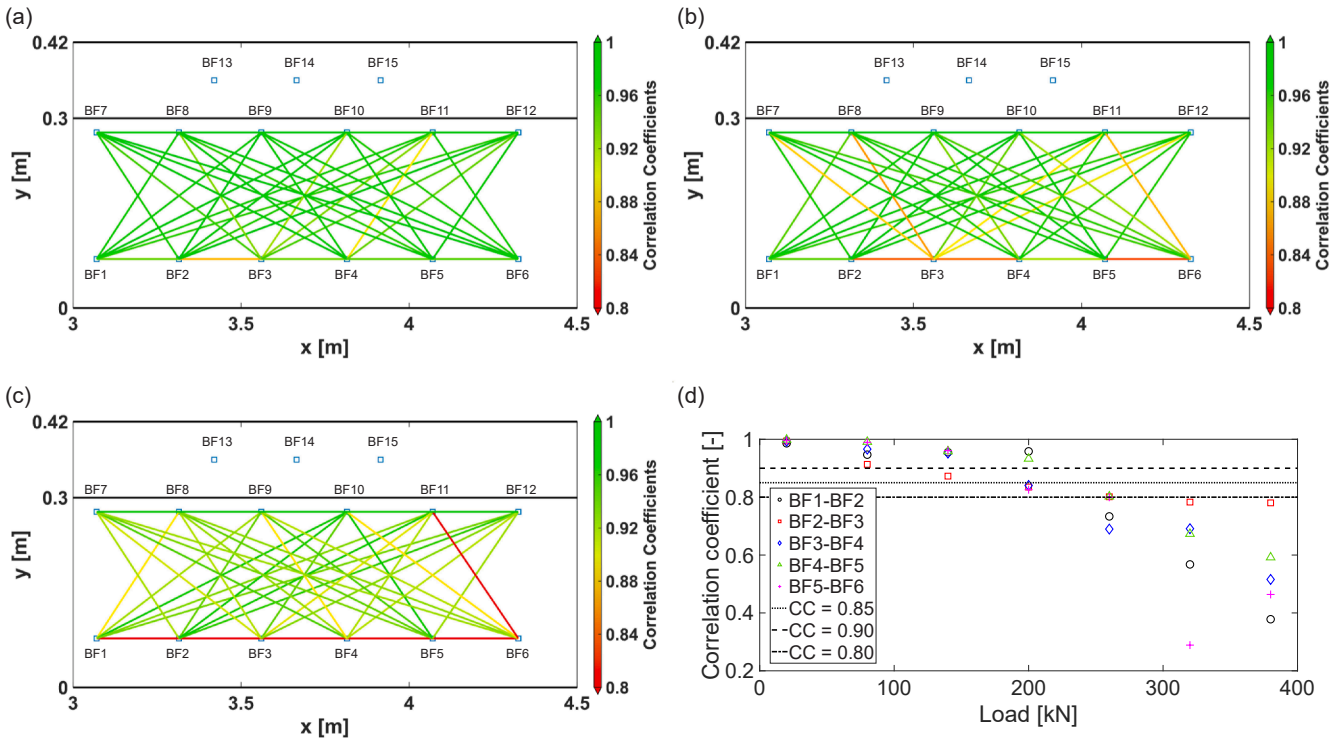

Fig. 18. *CC* values in the beam during the flexural test. (a) *CC* values within the sensor network at 140 kN (blue rectangles indicate sensors). (b) *CC* values within the sensor network at 200 kN (blue rectangles indicate sensors). (c) *CC* values within the sensor network at 260 kN (blue rectangles indicate sensors). (d) *CC* values vs. applied load for selected sensor pairs.

Proof load testing consists of applying a controlled load to the structure, usually up to a prescribed fraction of its expected capacity, to verify whether the bridge can safely sustain SLS or ULS demands. The test is terminated before unacceptable structural damage occurs, while continuous monitoring of deflections, strains, and crack opening is used to ensure safety. Here, crack opening refers to the re-opening of pre-existing closed cracks. Project-specific DI thresholds can be calibrated in the laboratory before conducting the proof load testing. There are four key requirements for the calibration testing. First, components should be made with the same, or at least representative, concrete mixture and curing conditions as those of the concrete used in the real bridge. Second, the cross-sectional dimension of the component should preferably be the same as that of the real bridge component to be tested. If this is not feasible, the cross-sectional dimension should be sufficiently large so that the analysed waveform is not dominated by boundary reflections, provided that the selected time window used for waveform coherency analysis in the real bridge does not contain many boundary reflections, as in the case presented in this paper. Third, component-level loading tests should be designed to reproduce the stress state of the monitored bridge cross section under the target proof-load level. Fourth, the number of embedded sensors adopted in the calibration testing can be less than those adopted in the field application; however, it is recommended that the sensor spacing and the distance from the sensors to the surface of the component be comparable to those adopted in the field. If the indicative DI thresholds were unexpectedly reached during proof loading, which should not occur at the relatively low load levels used, this would reveal the presence of pre-existing cracks and highlight the need for remedial measures to prevent further deterioration. During proof load testing, the initial unloaded state can be adopted as a test-specific baseline: relative wave velocity is referenced to this state, whereas the first *CC* value is obtained by comparing the signal recorded at the first loading stage with that measured in the unloaded condition. Additionally, measurements from sensors in the compression zone are recommended as control measurements to track stress-, noise-, and environment-related effects, because the concrete in this region is typically expected to remain uncracked during the test. In this context, the compression-zone measurements are intended primarily as test-specific control measurements during proof loading, rather than as a permanent baseline for the entire service life. For lifetime monitoring, baseline definition and updating are expected to require an adaptive interpretation framework that accounts for evolving environmental, operational, and material-related effects, which remains a subject for future research.

During proof load testing, a finite element (FE) model may play a crucial complementary role. First, it provides a framework to relate local DI measurements to the global behaviour of the bridge, thereby enabling a more comprehensive interpretation of the test data. Since DIs are tied to the location of the sensor network, they are inherently local and may only represent the condition of the monitored region. By contrast, the FE model allows the assessment to extend to unmonitored zones. Second, the two approaches can serve as mutual validation tools: if DI trends agree with the FE-predicted responses, confidence in both the measurements and the model is strengthened; conversely, marked discrepancies may indicate modelling inaccuracies or reveal hidden structural anomalies. Thus, combining DIs with FE analysis not only enhances the reliability of proof load testing but also broadens the scope of condition assessment beyond the immediate vicinity of the installed sensors.

Before these DIs can be used routinely in practice, their performance should ideally be calibrated in a more formal framework, both in terms of threshold selection (to control false positives and false negatives) and in terms of detection capability (minimum detectable crack size and orientation). In principle, receiver operating characteristic (ROC) analysis [104–106] could be employed to quantify the trade-off between detection and false-alarm rates and to identify optimal threshold levels. However, such an analysis requires independent crack labels at the level of individual sensor paths and load steps, as well as controlled

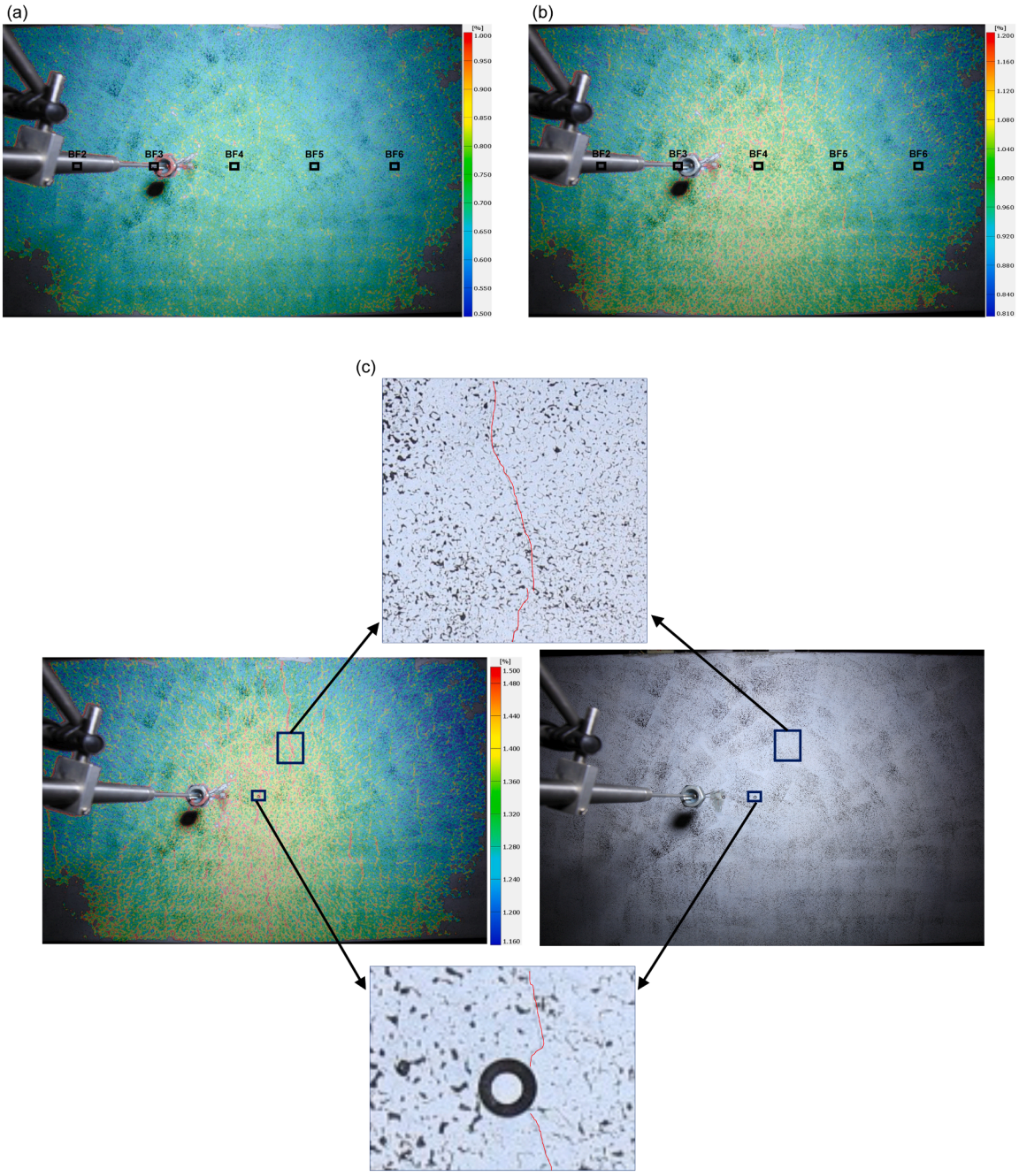

Fig. 19. DIC observation on the bottom surface of the beam for the flexural test at different load levels. (a) 140 kN. (b) 200 kN. (c) Comparison between the DIC result and a test image at 260 kN.

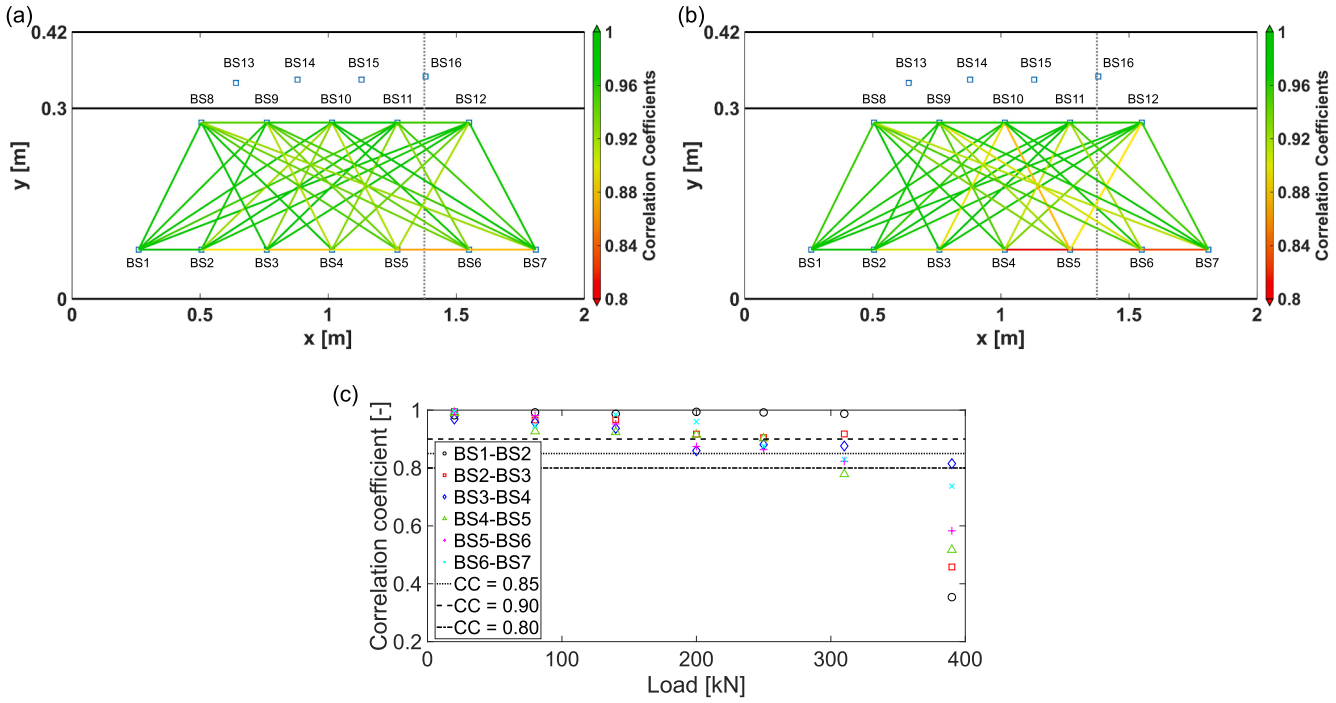

Fig. 20. *CC* values in the beam during the shear test. (a) *CC* values within the sensor network at 250 kN (blue rectangles indicate sensors; the black dotted line indicates the loading position). (b) *CC* values within the sensor network at 310 kN (blue rectangles indicate sensors; the black dotted line indicates the loading position). (c) *CC* values vs. applied load for selected sensor pairs.

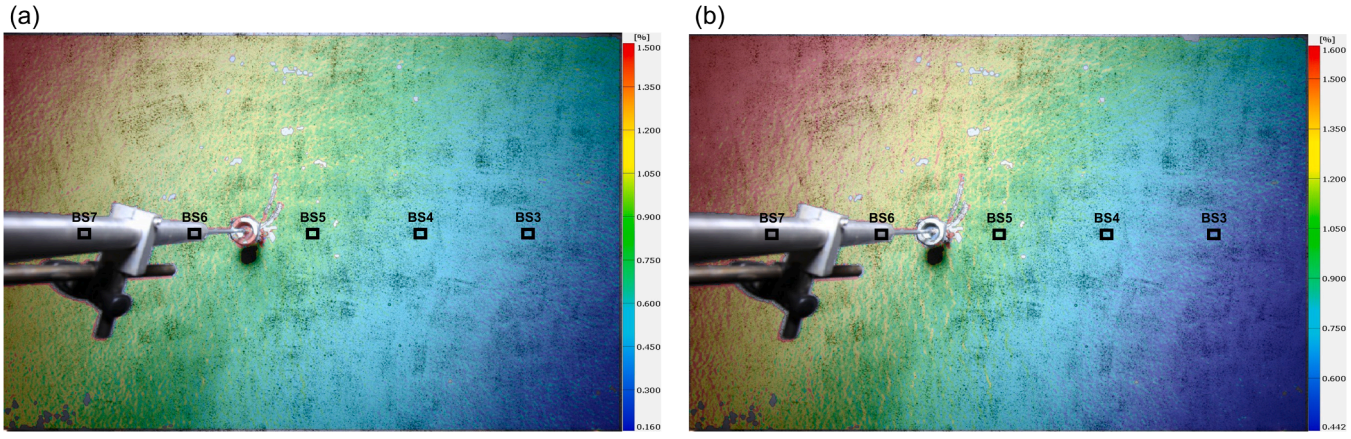

Fig. 21. DIC observation on the bottom surface of the beam for the shear test at different load levels. (a) 310 kN. (b) 390 kN.

information on crack geometry. For full-scale AAC bridge members with embedded sensors presented in this study, this is not experimentally achievable, because internal cracking along the wave paths cannot be directly observed and interface cracks under the topping cannot be characterized in a systematic way. As a consequence, the present study interprets the DIs at the level of cracked versus uncracked behaviour of monitored cross sections and does not attempt to quantify a minimum detectable crack size or a formal detection probability, which is a limitation of the current work. Future research will therefore focus on smaller, more controllable specimens and/or numerical simulations with fully known crack sizes and orientations, for which ROC-based optimization of *CC* and relative-velocity thresholds and systematic assessment of detection limits under different stress and environmental conditions can be carried out.

Cycle skipping is an important signal-processing artefact that needs to be addressed in applications. In the stretching-based DWI approach, cycle skipping is fundamentally associated with the quality and coherency of the recorded waveforms. The most effective mitigation strategy is to improve acquisition quality, thereby reducing the likelihood of cycle skipping at the source. Accordingly, several practical measures can be adopted for field monitoring of bridges. First, the SNR can be increased by using contact-type transducers with stable coupling and, where permissible, increasing the excitation energy while remaining within the linear operating range of the piezoelectric sensor. Second, a lower excitation frequency (approximately 50 kHz) is advantageous in concrete because attenuation is reduced, which improves the coda-wave SNR and decreases the probability of cycle skipping. Third, cycle skipping can be further mitigated by reducing the measurement interval, where feasible, and by using stepwise referencing to limit waveform divergence between consecutive measurements. These

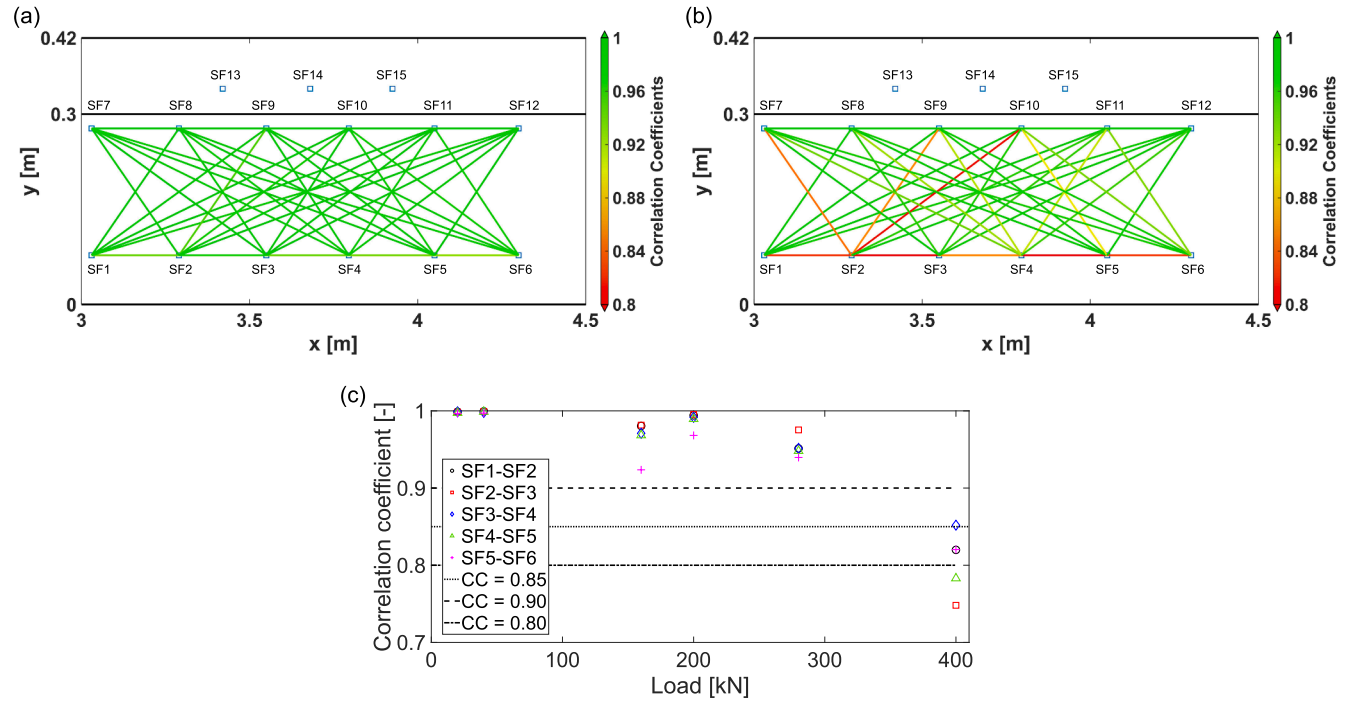

Fig. 22. *CC* values in the middle beam of the slab during the flexural test. (a) *CC* values within the sensor network at 280 kN (blue rectangles indicate sensors). (b) *CC* values within the sensor network at 400 kN (blue rectangles indicate sensors). (c) *CC* values vs. applied load for selected sensor pairs.

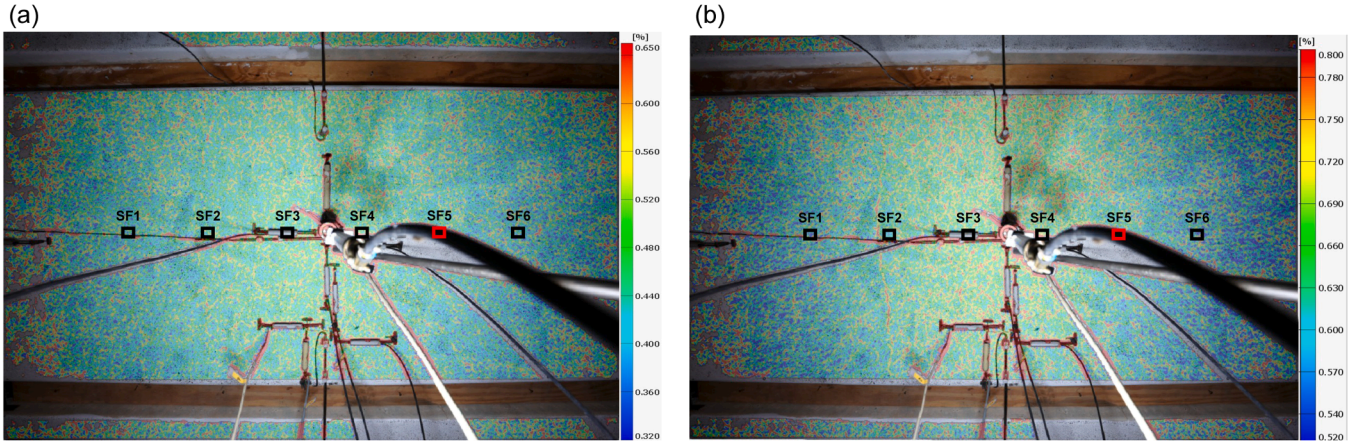

Fig. 23. DIC observation on the bottom surface of the middle beam during the flexural test at different load levels. (a) 280 kN. (b) 400 kN.

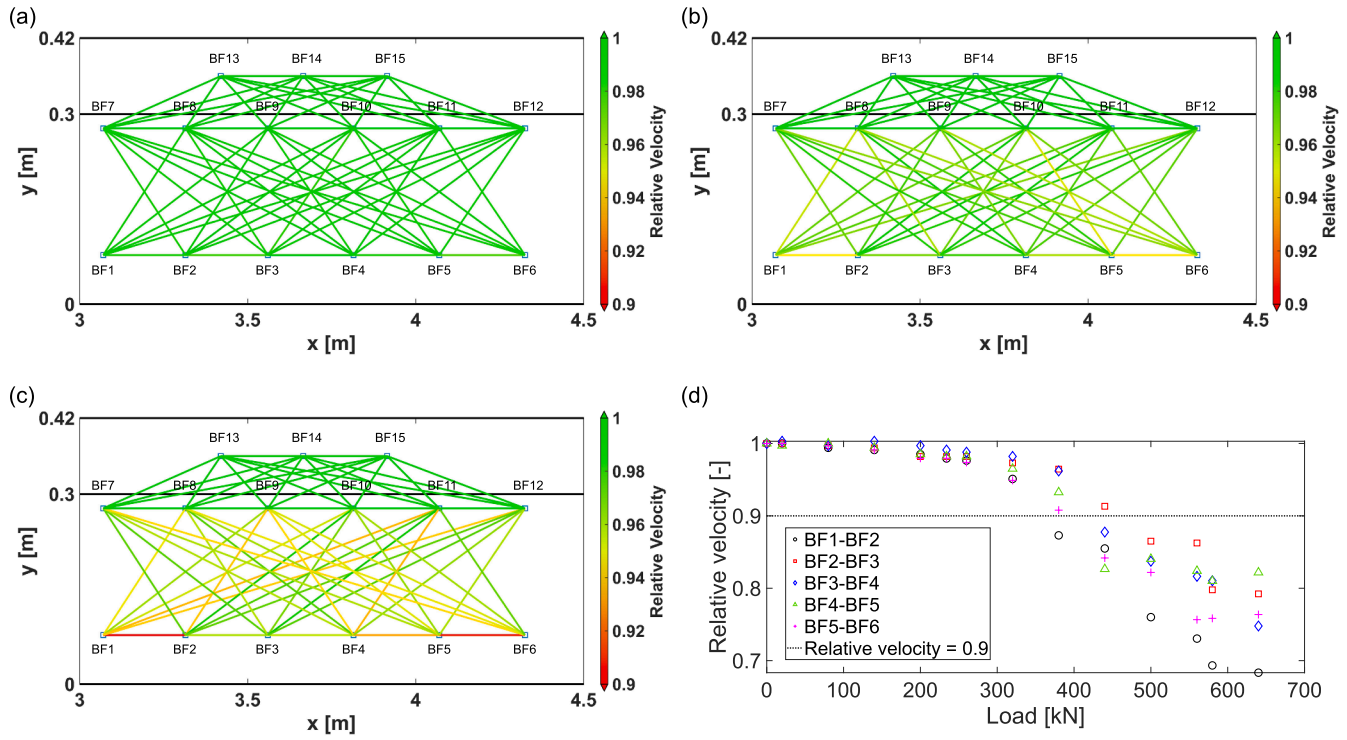

Fig. 24. Relative velocity in the beam during the flexural test. (a) Relative velocity within the sensor network at 200 kN (blue rectangles indicate sensors). (b) Relative velocity within the sensor network at 320 kN (blue rectangles indicate sensors). (c) Relative velocity within the sensor network at 380 kN (blue rectangles indicate sensors). (d) Relative velocity vs. applied load for selected sensor pairs.

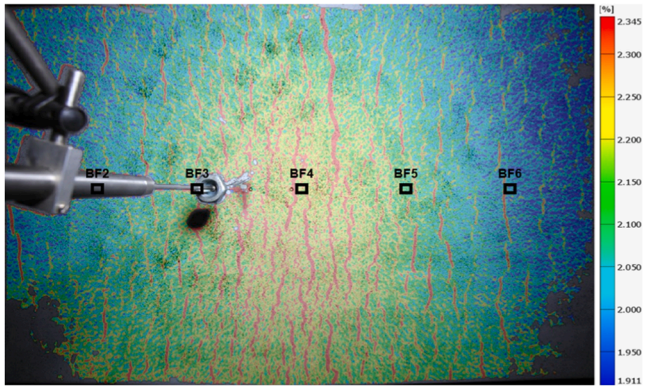

Fig. 25. DIC observation on the bottom surface of the beam for the flexural test at 380 kN.

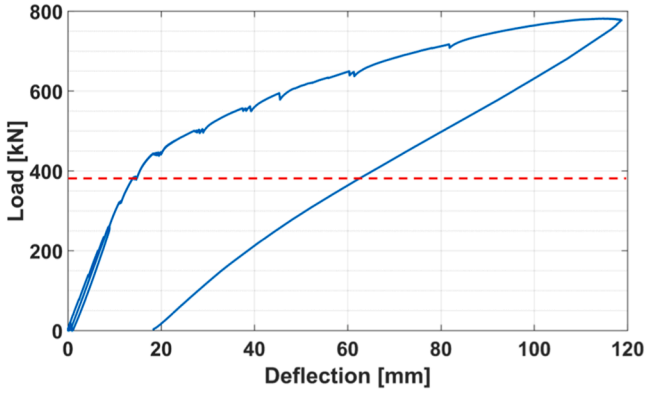

Fig. 26. Load-deflection curve at the midspan during the beam flexural test (the red dashed line corresponds to the load level of 380 kN).

acquisition measures should be complemented by automated quality-control procedures. In particular, SNR-based screening can be applied to reject propagation paths or time windows with SNR below a pre-defined threshold prior to DWI analysis. In addition, the stretching technique should be evaluated over multiple time windows to verify the consistency of the estimated velocity change. Specifically, velocity changes can be computed for all windows beginning at the first arrival, and estimates exhibiting anomalously large jumps or strong window-to-window inconsistency can be flagged for exclusion or re-fitting.

6.4. *Sensitivity of DIs to specimen geometry and concrete type*

The proposed DIs, namely waveform coherency and relative velocity, exhibit different levels of sensitivity to specimen geometry. Waveform coherency is strongly affected by geometrical conditions, since the choice of time window must be carefully adapted to the cross-sectional dimension of the specimen in order to adequately capture the changes in the target region. In contrast, the relative velocity indicator focuses only on the first arrival of the direct wave and is therefore less sensitive to specimen cross-sectional dimensions than waveform coherency.

With respect to material dependence, both indicators are in principle applicable to different concrete types, including AAC and conventional concrete. As reported in recent work on AAC, the strength and cracking behaviour of AAC depend on a number of mix-design and curing parameters, such as precursor type and content, water-to-binder ratio, and curing regime [107–109]. These effects can be understood in two categories: (1) baseline material-state effects and (2) crack-evolution effects. First, variations in precursor, liquid-to-binder ratio, curing regime and age can change porosity and reaction products, which affect baseline wave velocity, dispersion and attenuation (i.e., the waveform

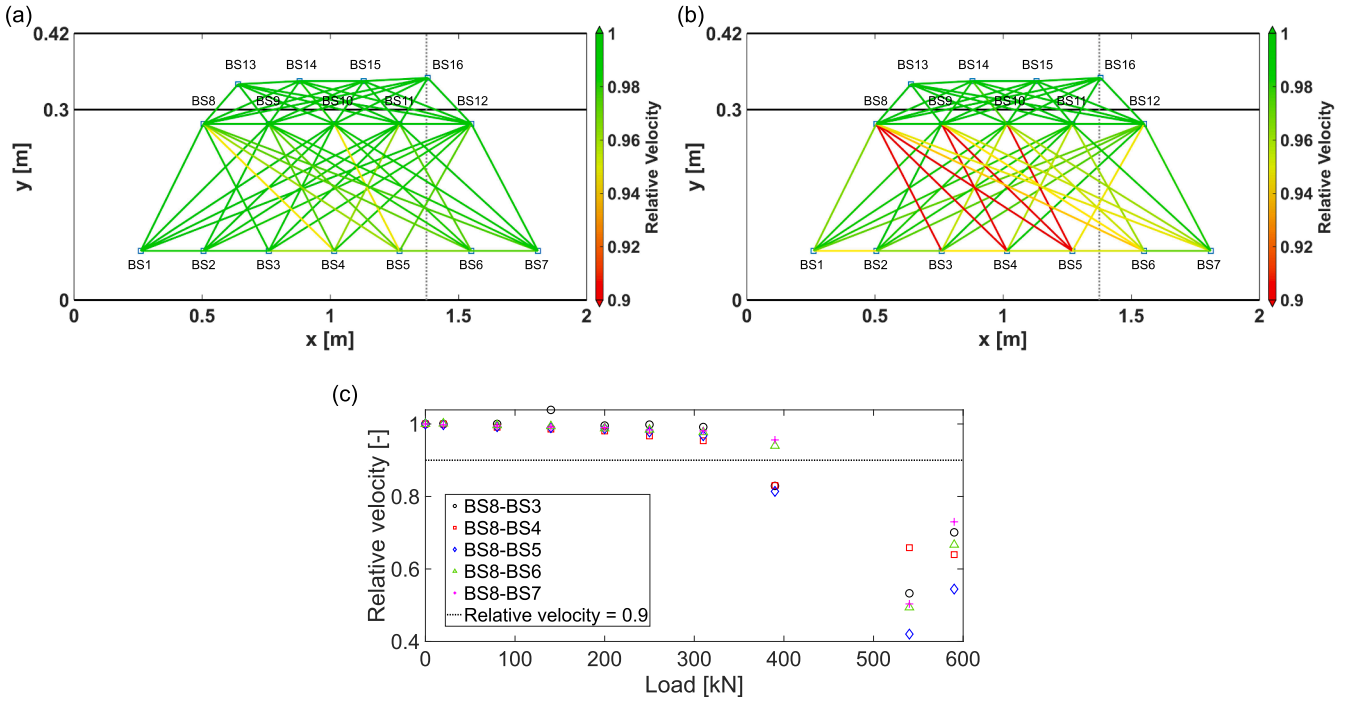

Fig. 27. Relative velocity in the beam during the shear test. (a) Relative velocity within the sensor network at 310 kN (blue rectangles indicate sensors; the black dotted line indicates the loading position). (b) Relative velocity within the sensor network at 390 kN (blue rectangles indicate sensors; the black dotted line indicates the loading position). (c) Relative velocity vs. applied load for selected sensor pairs.

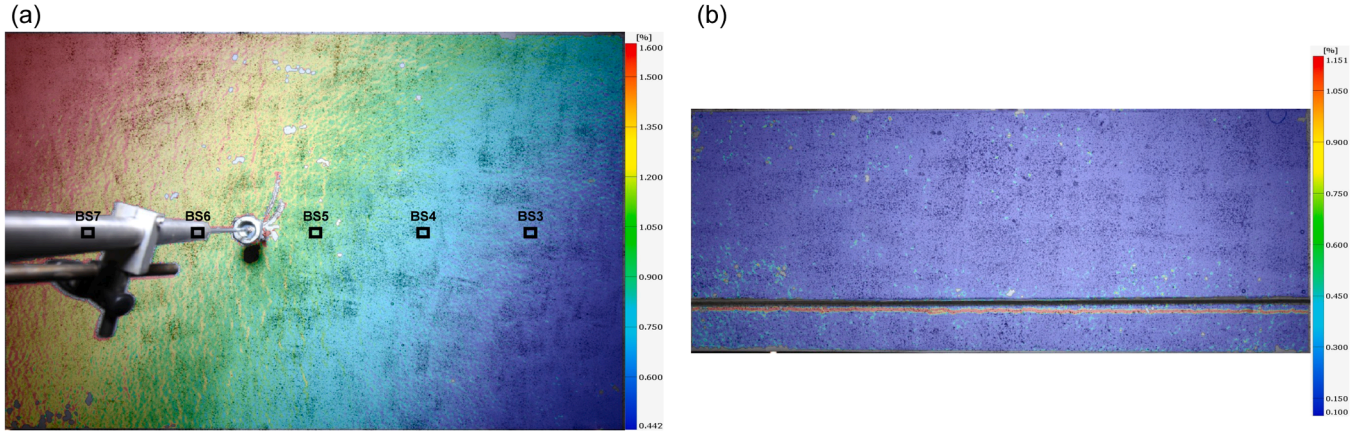

Fig. 28. DIC images on the beam during the shear test at 390 kN. (a) Bottom surface. (b) Side surface.

characteristics prior to cracking). Second, variations in tensile strength, fracture energy and, if applicable, fibre bridging can modify the crack pattern (distributed microcracking versus fewer wider cracks), crack opening and crack-growth rate. However, these variations do not invalidate the fundamental principle of damage indicators that (i) crack initiation is associated with a marked loss of waveform coherency, and (ii) extensive crack growth leads to a significant reduction in apparent wave velocity along affected paths.

For bridges made with different AAC mixtures or with conventional Portland cement concrete, the same ultrasonic DIs can therefore still be applied, but the quantitative DI thresholds corresponding to SLS and ULS must be recalibrated for the specific material and structure, in practice using project-specific material tests combined with structural tests in which the onset of cracking and relevant limit states are identified independently by conventional means. This suggests that future work should focus on systematic threshold determination to extend the applicability of the proposed indicators across a wider range of concrete materials and structural configurations. Even though the associated threshold values need to be calibrated for each specific bridge configuration, the experimental results indicate that, within the tested members, the two proposed DIs can provide early warning of stiffness degradation and allow typical flexural and shear failure mechanisms to be monitored when sensors are embedded at key cross sections. At the same time, the present findings are based on a limited number of full-scale specimens and do not yet include a formal statistical assessment of indicator variability or a fully quantitative validation against crack width, crack depth or prestress loss; these aspects will require further experimental and modelling work before the indicators can be used in a statistically calibrated framework.

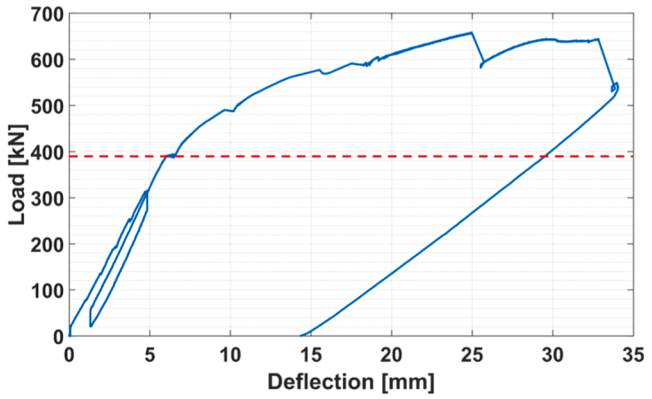

Fig. 29. Load-deflection curve at the loading point during the beam shear test (the red dashed line corresponds to the load level of 390 kN).

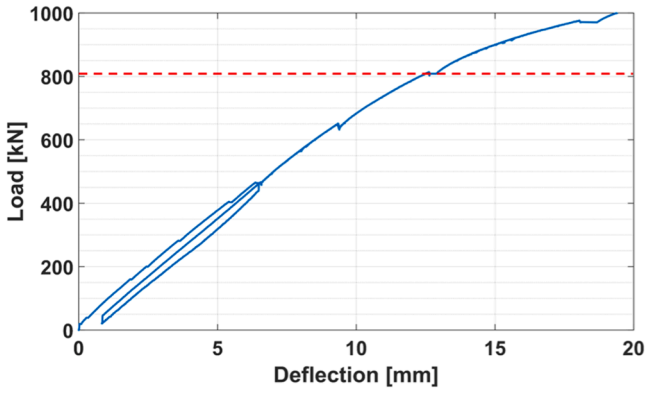

Fig. 31. Load-deflection curve at the midspan during the slab flexural test (the red dashed line corresponds to the load level of 810 kN).

6.5. *Future applications of multi-indicator cooperative monitoring*

In the literature on structural health monitoring and bridge performance assessment, traditional damage and performance indicators (e.g., condition index, deterioration index, structural safety indicator, traffic safety indicator) primarily serve to evaluate the residual life, serviceability and maintenance priority of entire structural components, systems or networks [13–16]. These indicators most often derive from visual inspections, non-destructive testing or monitoring systems, and are applied at relatively coarse spatial or temporal resolutions. By contrast, the two indicators proposed in this study are designed specifically to detect and quantify the early evolution of cracks as well as structural degradation under both SLS and ULS. Through quantifying waveform coherency and relative velocity, they enable higher-resolution monitoring of damage onset and progression. In doing so, these indicators complement the existing macro-level indices by filling the gap between microscopic damage initiation and macroscopic performance loss. While direct quantitative comparison with established indicators remains the subject of future work, this study contributes a new monitoring capability that can be integrated into a multi-indicator cooperative monitoring framework for enhanced validation, coverage of different resolutions, and improved decision-support in bridge management.

From a practical implementation perspective, however, the proposed embedded ultrasonic DI method should not be viewed as a replacement for conventional bridge assessment and SHM techniques, but rather as a complementary tool with a distinct role in monitoring critical local regions. In engineering practice, its added value must be considered together with factors such as installation effort, suitability for continuous monitoring, operation and maintenance requirements, data acquisition and interpretation complexity, and the ability to detect internal cracking. To clarify the practical positioning of the proposed method, Table 8 provides a qualitative comparison with periodic visual inspection, proof load testing, and distributed fibre-optic sensing.

In terms of *installation cost*, periodic visual inspection and proof load testing do not require permanent sensor installation on the bridge, whereas both the proposed ultrasonic method and distributed fibre-optic sensing require sensors to be installed in advance on or within the structure. The installation cost of the proposed ultrasonic method is therefore higher than that of visual inspection and proof load testing, but is often expected to be lower than that of distributed fibre-optic sensing in the type of application considered here, particularly because DFOS commonly requires a more expensive interrogator system; however, the actual cost will depend on project-specific instrumentation scale and installation requirements. In terms of *operation cost*, the proposed ultrasonic method and distributed fibre-optic sensing can be repeatedly used once installed, whereas periodic visual inspection requires dedicated personnel for repeated inspections, and proof load testing requires traffic control, loading equipment, and additional instrumentation such as LVDTs and strain gauges for each test; therefore, proof load testing has the highest event-based operation cost. Please note that, once the system has been installed, the per-measurement operational cost of the ultrasonic method may be relatively low. However, long-term maintenance, sensor reliability, and data interpretation still require dedicated effort. Regarding *potential suitability for continuous acquisition*, both the proposed ultrasonic method and distributed fibre-optic sensing are suitable for repeated long-term data acquisition after installation, although the interpretation of long-term measurements remains challenging because measurements may reflect coupled effects from structural, environmental, and operational influences. By contrast, periodic visual inspection and proof load testing are more suitable for periodic or event-based assessment. In terms of *data acquisition and interpretation*

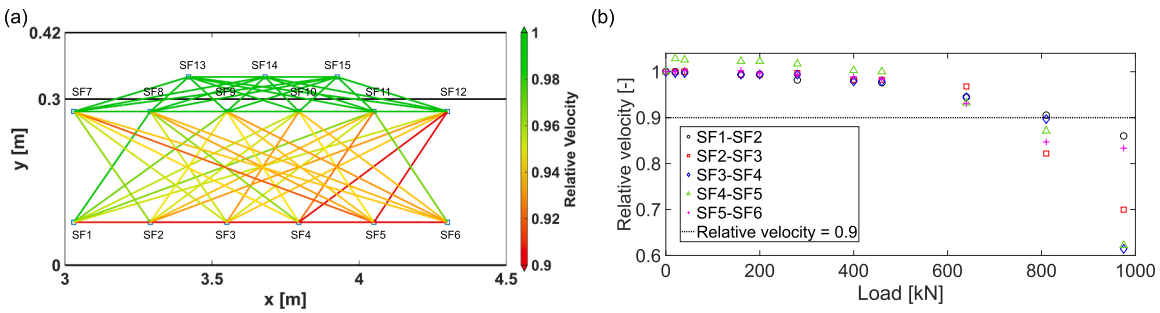

Fig. 30. Relative velocity in the middle beam of the slab during the flexural test. (a) Relative velocity within the sensor network at 810 kN (blue rectangles indicate sensors). (b) Relative velocity vs. applied load for selected sensor pairs.

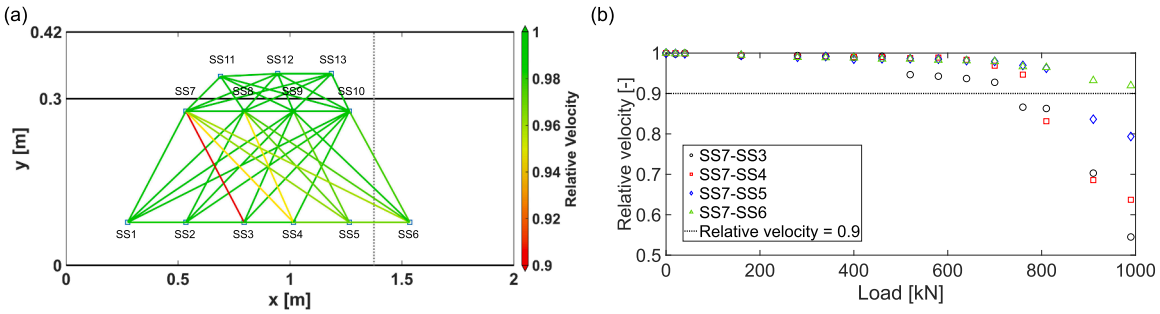

Fig. 32. Relative velocity in the side beam of the slab during the shear test. (a) Relative velocity within the sensor network at 760 kN (blue rectangles indicate sensors; the black dotted line indicates the loading position). (b) Relative velocity vs. applied load for selected sensor pairs.

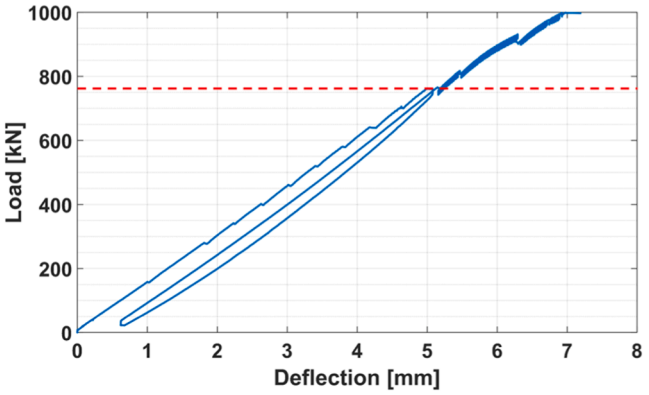

Fig. 33. Load-deflection curve under the beam with sensor embedded during the slab shear test (the red dashed line corresponds to the load level of 760 kN).

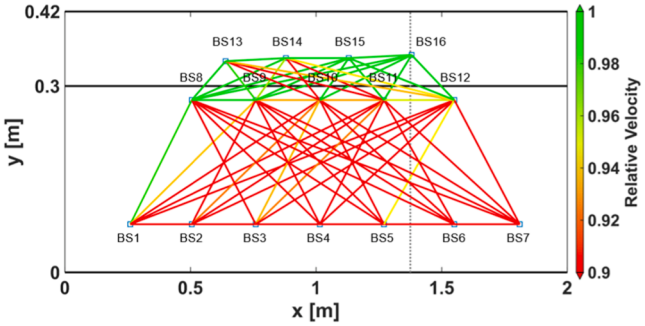

Fig. 34. Relative velocity within the sensor network in the beam for the shear test at 590 kN (blue rectangles indicate sensors; the black dotted line indicates the loading position).

complexity, the proposed ultrasonic method is the most demanding because it requires both signal processing of the acquired waveforms and subsequent interpretation of the derived DIs with respect to structural behaviour. In comparison, the displacement and strain data obtained during proof load testing and the strain data obtained by fibre-optic sensing can be used more directly for structural assessment, whereas periodic visual inspection has the lowest interpretation complexity. With respect to the *ability to detect internal cracking*, the proposed embedded ultrasonic method has a clear advantage because an array of embedded sensors can directly investigate the interior of the structural member. Periodic visual inspection cannot detect internal damage, and proof load testing by itself cannot directly identify internal cracking unless combined with additional sensing techniques. Distributed fibre-optic sensing can provide some sensitivity to cracking, but this depends strongly on the sensor location, since this method is mainly sensitive to cracking occurring close to the sensing path. In terms of *spatial coverage*, the proposed ultrasonic method and distributed fibre-optic sensing are both local methods, the former being focused on instrumented critical sections and the latter along the installed sensing line. By contrast, periodic visual inspection provides a more global condition assessment, while proof load testing supports assessment at the structural level because displacement and strain measurements can be collected at several critical locations.

Overall, the practical role of the proposed method is not to replace existing approaches, but to complement them. In particular, a proof-load-assisted multi-sensor assessment strategy appears especially suitable at the current stage, in which embedded ultrasonic DIs may be combined with distributed fibre-optic sensing and conventional measurements such as LVDTs. Such a strategy allows multiple complementary indicators to be established and cross-validated, thereby improving redundancy and confidence in the assessment results. Since proof load testing cannot be performed frequently, periodic visual inspection can serve as a practical supplementary approach between proof load tests.

Table 8
Qualitative comparison of the proposed embedded ultrasonic DI method with selected bridge assessment and monitoring approaches.

Method	Proposed embedded ultrasonic DI method	Periodic visual inspection	Proof load testing	Distributed fibre-optic sensing
Installation cost	Moderate	Low	Low	High
Operation cost	Low to moderate	Moderate	High	Low
Potential suitability for continuous acquisition	Yes	No	No	Yes
Data acquisition and interpretation complexity	High	Low	Moderate	Moderate
Ability to detect internal cracking	High	Poor	Indirect only	Moderate
Spatial coverage	Local, concentrated at instrumented critical sections	Global	Global	Local along sensing line

7. Conclusion

This paper outlines a series of laboratory tests conducted on AAC bridge elements with the aim of proposing DIs for future long-term monitoring applications. Embeddable ultrasonic sensors are employed to generate and detect elastic waves in concrete. The use of these sensors enables the tracking of crack initiation and propagation within the present full-scale tests on AAC bridge components, a capability that is difficult to achieve using surface-based measurement techniques alone. The experiments involved two prestressed AAC composite beams and a solid slab comprising three beams. Based on the test outcomes, we

identified two key structural DIs tailored for the long-term monitoring of precast AAC slab bridges using embedded sensors:

- The first DI is based on the reduction in waveform coherency, specifically targeting the detection of crack initiation in the precast beam, and also serves as a means to assess SLS.
- The second DI, based on relative velocity, aims to detect crack propagation in the precast beam. It functions as an early warning for deterioration of flexural behaviour at the critical cross section of the slab strip, as well as potential brittle shear failure caused by shear crack propagation in the shear-critical zone.

Within the present full-scale tests on AAC bridge components, these two ultrasonic indicators consistently correlated with the observed crack development and changes in global structural response, indicating that they are promising indicators for distinguishing, within the present controlled tests, between SLS-related crack initiation and more advanced damage states when sensors are embedded at key cross sections. However, the threshold values identified in this study are specific to the investigated AAC system, geometry and loading conditions and should be regarded as indicative rather than universal. Application of the proposed framework to other AAC mixtures, geometries or conventional concrete bridges will require project-specific calibration and additional experimental and modelling verification.

Supplementary material

Plots of the *CC* and relative velocity for each measurement are available in the supplementary material.

CRediT authorship contribution statement

Yuguang Yang: Writing – review & editing, Supervision, Resources, Project administration, Funding acquisition, Conceptualization. **Guang Ye:** Writing – review & editing, Resources, Project administration, Funding acquisition. **Zhenxu Qian:** Writing – review & editing, Visualization. **Shizhe Zhang:** Writing – review & editing, Visualization, Investigation, Formal analysis. **Hao Cheng:** Writing – original draft, Visualization, Validation, Software, Methodology, Investigation, Formal analysis, Data curation.

Declaration of Competing Interest

The authors declare that they have no known competing financial interests or personal relationships that could have appeared to influence the work reported in this paper.

Appendix A. Supporting information

Supplementary data associated with this article can be found in the online version at doi:10.1016/j.engstruct.2026.122675.

Data availability

Data will be made available on request.

References

[1] Schneider M. The cement industry on the way to a low-carbon future. Cem Concr Res 2019;124:105792. https://doi.org/10.1016/j.cemconres.2019.105792.
[2] Friedlingstein P, O'sullivan M, Jones MW, et al. Global carbon budget 2023. Earth Syst Sci Data 2023;15:5301–69. https://doi.org/10.5194/essd-15-5301-2023.
[3] Stanëk T, Sulovský P. Active low-energy belite cement. Cem Concr Res 2015;68:203–10. https://doi.org/10.1016/j.cemconres.2014.11.004.
[4] Cuesta A, Ayuela A, Aranda MA. Belite cements and their activation. Cem Concr Res 2021;140:106319. https://doi.org/10.1016/j.cemconres.2020.106319.
[5] Tao Y, Rahul A, Mohan MK, et al. Recent progress and technical challenges in using calcium sulfoaluminate (CSA) cement. Cem Concr Compos 2023;137:104908. https://doi.org/10.1016/j.cemconcomp.2022.104908.
[6] Pooni J, Robert D, Giustozzi F, et al. Novel use of calcium sulfoaluminate (CSA) cement for treating problematic soils. Constr Build Mater 2020;260:120433. https://doi.org/10.1016/j.conbuildmat.2020.120433.
[7] Pacheco-Torgal F, Labrincha J, Leonelli C, et al. Handbook of alkali-activated cements, mortars and concretes. Elsevier; 2014. ISBN: 978-1-78242-276-1.
[8] Provis JL. Alkali-activated materials. Cem Concr Res 2018;114:40–8. https://doi.org/10.1016/j.cemconres.2017.02.009.
[9] Ding Y, Dai J, Shi C. Mechanical properties of alkali-activated concrete: A state-of-the-art review. Constr Build Mater 2016;127:68–79. https://doi.org/10.1016/j.conbuildmat.2016.09.121.
[10] Zhang P, Wang K, Li Q, et al. Fabrication and engineering properties of concretes based on geopolymers/alkali-activated binders-A review. J Clean Prod 2020;258:120896. https://doi.org/10.1016/j.jclepro.2020.120896.
[11] Amran YM, Alyousef R, Alabduljabbar H, et al. Clean production and properties of geopolymer concrete; A review. J Clean Prod 2020;251:119679. DOI: 0.1016/j.jclepro.2019.119679.
[12] Habert G, Ouellet-Plamondon C. Recent update on the environmental impact of geopolymers. RILEM Tech Lett 2016;1:17–23. https://doi.org/10.21809/rilemtechlett.2016.6.
[13] Strauss A., Mandić Ivanković A., Matos J.C., et al. Performance indicators for road bridges-overview of findings and future progress. 2017. DOI:
[14] Zanini MA, Faleschini F, Casas JR. State-of-research on performance indicators for bridge quality control and management. Front Built Environ 2019;5:22. https://doi.org/10.3389/fbuil.2019.00022.
[15] Marić MK, Ivanković AM, Srbić M, et al. Assessment of performance indicators of a large-span reinforced concrete arch bridge in a multi-hazard environment. Buildings 2022;12:1046. https://doi.org/10.3390/buildings12071046.
[16] Xia Y, Lei X, Wang P, et al. Long-term performance monitoring and assessment of concrete beam bridges using neutral axis indicator. Struct Control Health Monit 2020;27:e2637. https://doi.org/10.1002/stc.2637.
[17] Yang Y, den Uijl J, Walraven J. Critical shear displacement theory: on the way to extending the scope of shear design and assessment for members without shear reinforcement. Struct Concr 2016;17:790–8. https://doi.org/10.1002/suco.201500135.
[18] Cavagnis F, Ruiz MF, Muttoni A. Shear failures in reinforced concrete members without transverse reinforcement: An analysis of the critical shear crack development on the basis of test results. Eng Struct 2015;103:157–73. https://doi.org/10.1016/j.engstruct.2015.09.015.
[19] Deraemaeker A, Dumoulin C. Embedding ultrasonic transducers in concrete: A lifelong monitoring technology. Constr Build Mater 2019;194:42–50. https://doi.org/10.1016/j.conbuildmat.2018.11.013.
[20] Rizzo P, Enshaeian A. Bridge health monitoring in the United States: A review. Structural Monitoring and Maintenance. Int J 2021;8:1–50. https://doi.org/10.12989/smm.2021.8.1.001.
[21] Majumder M, Gangopadhyay TK, Chakraborty AK, et al. Fibre Bragg gratings in structural health monitoring - Present status and applications. Sens Actuators A Phys 2008;147:150–64. https://doi.org/10.1016/j.sna.2008.04.008.
[22] Barrias A, Casas JR, Villalba S. A review of distributed optical fiber sensors for civil engineering applications. Sensors 2016;16:35. https://doi.org/10.3390/s16050748.
[23] Larose E, Hall S. Monitoring stress related velocity variation in concrete with a 2×10-5 relative resolution using diffuse ultrasound. J Acoust Soc Am 2009;125:1853–6. https://doi.org/10.1121/1.3079771.
[24] Wunderlich C. and Niederleithinger E. Evaluation of temperature influence on ultrasound velocity in concrete by coda wave interferometry. In: Güneş, O., Akkaya, Y. (eds) Nondestructive Testing of Materials and Structures. RILEM Bookseries, vol 6. Springer, Dordrecht. DOI: ⟨10.1007/978-94-007-0723-8_33⟩.
[25] Vu G, Timothy JJ, Saenger EH, et al. A virtual lab for damage identification in concrete using coda wave interferometry. Struct Infrastruct Eng 2025:1–16. https://doi.org/10.1080/15732479.2025.2474699.
[26] Liu PC. Wavelet spectrum analysis and ocean wind waves. Wavelet Analysis and Its Applications, 4. Elsevier; 1994. p. 151–66. https://doi.org/10.1016/B978-0-08-052087-2.50012-8.
[27] Karaiskos G, Deraemaeker A, Aggelis DG, et al. Monitoring of concrete structures using the ultrasonic pulse velocity method. Smart Mater Struct 2015;24:18. https://doi.org/10.1088/0964-1726/24/11/113001.
[28] Breysse D. Nondestructive evaluation of concrete strength: An historical review and a new perspective by combining NDT methods. Constr Build Mater 2012;33:139–63. https://doi.org/10.1016/j.conbuildmat.2011.12.103.
[29] Selleck SF, Landis EN, Peterson ML, et al. Ultrasonic investigation of concrete with distributed damage. Acids Mater J 1998;95:27–36. https://doi.org/10.14359/349.
[30] Chai H, Momoki S, Kobayashi Y, et al. Tomographic reconstruction for concrete using attenuation of ultrasound. NDT & E Int 2011;44:206–15. https://doi.org/10.1016/j.ndteint.2010.11.003.
[31] Zhou L, Zheng Y, Ma H, et al. Attenuation characteristics of stress wave in cracked concrete beam using smart aggregate transducers enabled time-reversal technique. J Intell Mater Syst Struct 2021;32:473–85. https://doi.org/10.1177/1045389X2095361.
[32] Gong P, Song P, Huang C, et al. Noise suppression for ultrasound attenuation coefficient estimation based on spectrum normalization. IEEE Trans Ultrason Ferroelectr Freq Control 2021;68:2667–74. https://doi.org/10.1109/TUFFC.2021.3074293.

[33] van Den Abeele K, Desadeleer W, De Schutter G, et al. Active and passive monitoring of the early hydration process in concrete using linear and nonlinear acoustics. Cem Concr Res 2009;39:426–32. https://doi.org/10.1016/j.cemconres.2009.01.016.

[34] Yang C, Chen J. Fully noncontact nonlinear ultrasonic characterization of thermal damage in concrete and correlation with microscopic evidence of material cracking. Cem Concr Res 2019;123:105797. https://doi.org/10.1016/j.cemconres.2019.105797.

[35] Climent MÁ, Miró M, Carbajo J, et al. Use of non-linear ultrasonic techniques to detect cracks due to steel corrosion in reinforced concrete structures. Materials 2019;12:813. https://doi.org/10.3390/ma12050813.

[36] Climent MÁ, Miró M, Poveda P, et al. Use of higher-harmonic and intermodulation generation of ultrasonic waves to detecting cracks due to steel corrosion in reinforced cement mortar. Int J Concr Struct Mater 2020;14:52. https://doi.org/10.1186/s40069-020-00432-x.

[37] Climent MÁ, Miró M, Eiras JN, et al. Early detection of corrosion-induced concrete micro-cracking by using nonlinear ultrasonic techniques: Possible influence of mass transport processes. Corros Mater Degrad 2022;3:235–57. https://doi.org/10.3390/cmd3020014.

[38] Lissenden CJ. Nonlinear ultrasonic guided waves—Principles for nondestructive evaluation. J Appl Phys 2021;129.

[39] Yi S, Yang C, Sun X, et al. Evaluation of compressive damage in concrete using ultrasonic nonlinear coda wave interferometry. Ultrasonics 2024;144:107438. https://doi.org/10.1016/j.ultras.2024.107438.

[40] Zhan H, Jiang H, Liang Z, et al. Nondestructive in situ imaging of preexisting cracks in a concrete bridge using ultrasonic coda wave. J Struct Eng 2023;149:04022215. https://doi.org/10.1061/JSENDH.STENG-11299.

[41] Qu S, Hilloulin B, Saliba J, et al. Imaging concrete cracks using nonlinear Coda Wave Interferometry (INCWI). Constr Build Mater 2023;391:131772. https://doi.org/10.1016/j.conbuildmat.2023.131772.

[42] Sun M, Xu W, Zheng K, et al. Research on damage and stress monitoring analysis of cement-based materials based on integrated sensing element (ISE). Case Stud Constr Mater 2025:e04789. https://doi.org/10.1016/j.cscm.2025.e04789.

[43] Zhong B, Zhu J, Morcous G. Measuring acoustoelastic coefficients for stress evaluation in concrete. Constr Build Mater 2021;309:125127. https://doi.org/10.1016/j.conbuildmat.2021.125127.

[44] Zhang Y, Abraham O, Tournat V, et al. Validation of a thermal bias control technique for Coda Wave Interferometry (CWI). Ultrasonics 2013;53:658–64. https://doi.org/10.1016/j.ultras.2012.08.003.

[45] Zotz-Wilson R, Boerrigter T, Barnhoorn A. Coda-wave monitoring of continuously evolving material properties and the precursory detection of yielding. J Acoust Soc Am 2019;145:1060–8. https://doi.org/10.1121/1.5091012.

[46] Lobkis OI, Weaver RL. Coda-wave interferometry in finite solids: recovery of P-to-S conversion rates in an elastodynamic billiard. Phys Rev Lett 2003;90:254302. https://doi.org/10.1103/PhysRevLett.90.254302.

[47] Nguyen NT, Sbartaï ZM, Lataste JF, et al. Assessing the spatial variability of concrete structures using NDT techniques-Laboratory tests and case study. Constr Build Mater 2013;49:240–50. https://doi.org/10.1016/j.conbuildmat.2013.08.011.

[48] Larose E, Planes T, Rossetto V, et al. Locating a small change in a multiple scattering environment. Appl Phys Lett 2010;96:204101. https://doi.org/10.1063/1.3431269.

[49] Hilloulin B, Zhang Y, Abraham O, et al. Small crack detection in cementitious materials using nonlinear coda wave modulation. NDT & E Int 2014;68:98–104. https://doi.org/10.1016/j.ndteint.2014.08.010.

[50] Zhang Y, Planes T, Larose E, et al. Diffuse ultrasound monitoring of stress and damage development on a 15-ton concrete beam. J Acoust Soc Am 2016;139:1691. https://doi.org/10.1121/1.4945097.

[51] Legland JB, Zhang Y, Abraham O, et al. Evaluation of crack status in a meter-size concrete structure using the ultrasonic nonlinear coda wave interferometry. J Acoust Soc Am 2017;142:2233. https://doi.org/10.1121/1.5007832.

[52] Larose E, Obermann A, Digulescu A, et al. Locating and characterizing a crack in concrete with diffuse ultrasound: A four-point bending test. J Acoust Soc Am 2015;138:232–41. https://doi.org/10.1121/1.4922330.

[53] Hadziioannou C, Larose E, Coutant O, et al. Stability of monitoring weak changes in multiply scattering media with ambient noise correlation: laboratory experiments. J Acoust Soc Am 2009;125:3688–95. https://doi.org/10.1121/1.3125345.

[54] Cheng H, Weemstra C, Hendriks MAN, et al. Comparing the stretching technique and the wavelet cross-spectrum technique for measuring stress-induced wave-velocity changes in concrete. Autom Constr 2024;158:105221. https://doi.org/10.1016/j.autcon.2023.105221.

[55] Planès T, Larose E. A review of ultrasonic Coda Wave Interferometry in concrete. Cem Concr Res 2013;53:248–55. https://doi.org/10.1016/j.cemconres.2013.07.009.

[56] Pahlavan L, Zhang F, Blacquière G, et al. Interaction of ultrasonic waves with partially-closed cracks in concrete structures. Constr Build Mater 2018;167:899–906. https://doi.org/10.1016/j.conbuildmat.2018.02.098.

[57] Schubnel A, Benson PM, Thompson BD, et al. Quantifying damage, saturation and anisotropy in cracked rocks by inverting elastic wave velocities. Pure Appl Geophys 2006:947–73. https://doi.org/10.1007/s00024-006-0061-y.

[58] Meglis I, Chow T, Martin C, et al. Assessing in situ microcrack damage using ultrasonic velocity tomography. Int J Rock Mech Min Sci 2005;42:25–34. https://doi.org/10.1016/j.ijrmms.2004.06.002.

[59] Anderson DL, Minster B, Cole D. The effect of oriented cracks on seismic velocities. J Geophys Res 1974;79:4011–5. https://doi.org/10.1029/JB079i026p04011.

[60] Saenger EH, Shapiro SA. Effective velocities in fractured media: a numerical study using the rotated staggered finite-difference grid. Geophys Prospect 2002;50:183–94. https://doi.org/10.1046/j.1365-2478.2002.00309.x.

[61] Kachanov M. Effective elastic properties of cracked solids: critical review of some basic concepts. Appl Mech Rev 1992;45(8):304–35. https://doi.org/10.1115/1.3119761.

[62] Davis PM, Knopoff L. The elastic modulus of media containing strongly interacting antiplane cracks. J Geophys Res Solid Earth 1995;100:18253–8. https://doi.org/10.1029/95JB00717.

[63] Zararis PD, Papadakis GC. Diagonal shear failure and size effect in RC beams without web reinforcement. J Struct Eng 2001;127:733–42. https://doi.org/10.1061/(ASCE)0733-9445(2001)127:7(733).

[64] Eshelby JD. The determination of the elastic field of an ellipsoidal inclusion, and related problems. Proc R Soc Lond Ser A 1957;241:376–96. https://doi.org/10.1098/rspa.1957.0133.

[65] Hudson J. Overall properties of a cracked solid. Math Proc Camb Philos Soc 1980;88(2):371–84. https://doi.org/10.1017/S0305004100057674.

[66] Hudson JA. Wave speeds and attenuation of elastic waves in material containing cracks. Geophys J Int 1981;64:133–50. https://doi.org/10.1111/j.1365-246X.1981.tb02662.x.

[67] Cheng C. Crack models for a transversely isotropic medium. J Geophys Res Solid Earth 1993;98:675–84. https://doi.org/10.1029/92JB02118.

[68] Guo J, Gurevich B. Frequency-dependent P wave anisotropy due to wave-induced fluid flow and elastic scattering in a fluid-saturated porous medium with aligned fractures. J Geophys Res Solid Earth 2020;125:e2020JB020320. https://doi.org/10.1029/2020JB020320.

[69] Hinkley DV. Inference about the change-point from cumulative sum tests. Biometrika 1971;58:509–23. https://doi.org/10.1093/biomet/58.3.509.

[70] Maeda N. A method for reading and checking phase times in autoprocessing system of seismic wave data. Zisin 1985;38:365–79.

[71] Kurz JH, Grosse CU, Reinhardt HW. Strategies for reliable automatic onset time picking of acoustic emissions and of ultrasound signals in concrete. Ultrasonics 2005;43:538–46. https://doi.org/10.1016/j.ultras.2004.12.005.

[72] Zhang H, Thurber C, Rowe C. Automatic-wave arrival detection and picking with multiscale wavelet analysis for single-component recordings. Bull Seismol Soc Am 2003;93:1904–12. https://doi.org/10.1785/0120020241.

[73] Espion B, Halleux P. Long term behavior of prestressed and partially prestressed concrete beams: experimental and numerical results. Spec Publ 1991;129:19–38. https://doi.org/10.14359/1321.

[74] Zhang S, Ye G, Lukovic M, et al. Geopolymeerbeton voor infrastructurele toepassingen (1): Ontwikkeling van zelfverdichtende mengsels. Cement 2022;2022:42–50.

[75] Ye G, Zhang S, Lukovic M, et al. Geopolymeerbeton voor infrastructurele toepassingen (2): Productie op industriële schaal van prefab voorgespannen brugliggers. Cement 2023;2023:6–12.

[76] Matthys S, Proia A. Loading tests on prestressed precast bridge deck members in AAM concrete. Test Report University of Ghent; 2022. Report number: 19IC-TUD-AAMslab/A20TT1547.

[77] Song G, Gu H, Mo YL, et al. Concrete structural health monitoring using embedded piezoceramic transducers. Smart Mater Struct 2007;16:959–68. https://doi.org/10.1088/0964-1726/16/4/003.

[78] Song G, Gu H, Mo YL. Smart aggregates: multi-functional sensors for concrete structures - a tutorial and a review. Smart Mater Struct 2008;17:17. https://doi.org/10.1088/0964-1726/17/3/033001.

[79] Kong Q. Innovation in Piezoceramic Based Structural Health Monitoring (Doctoral dissertation). University of Houston; 2015. ⟨http://hdl.handle.net/10657/3664⟩ (URL).

[80] Niederleithinger E, Wolf J, Mielentz F, et al. Embedded ultrasonic transducers for active and passive concrete monitoring. Sensors 2015;15:9756–72. https://doi.org/10.3390/s150509756.

[81] Huo L, Cheng H, Kong Q, et al. Bond-slip monitoring of concrete structures using smart sensors-a review. Sensors 2019;19:1231. https://doi.org/10.3390/s19051231.

[82] Qian Z, Zhang S, Ye G, et al. Time-dependent flexural behaviour of prestressed alkali-activated concrete (AAC) girder with cast-in-situ AAC topping. Constr Build Mater 2025;484:141615. https://doi.org/10.1016/j.conbuildmat.2025.141615.

[83] Qian Z, Luković M. Prestressed alkali-activated concrete (AAC) members with cast-in-situ AAC topping: Additional analysis of structural tests including dic measurements. Technical Report Delft University of Technology; 2022.

[84] Yang Y., van Beek C. and Cheng H. Smart aggregate for monitoring of concrete structures: design of embedded ultrasonic tomography system. 2025. International Application No.: PCT/NL2024/050597.

[85] Rossetto V, Margerin L, Planès T, et al. Locating a weak change using diffuse waves: Theoretical approach and inversion procedure. J Appl Phys 2011;109:034903. https://doi.org/10.1063/1.3544503.

[86] Cheng H, Löer K, Hendriks MAN, et al. Determining the acoustoelastic effect of longitudinal waves propagating inclined to principal stress directions in concrete: theory and experimental validation. NDT & E Int 2025:103519. https://doi.org/10.1016/j.ndteint.2025.103519.

[87] Lillamand I, Chaix JF, Ploix MA, et al. Acoustoelastic effect in concrete material under uni-axial compressive loading (Article) NDT & E Int 2010;43:655–60. https://doi.org/10.1016/j.ndteint.2010.07.001.

[88] Zhong B, Zhu J. Applications of stretching technique and time window effects on ultrasonic velocity monitoring in concrete. Appl Sci 2022;12:7130. https://doi.org/10.3390/app12147130.
[89] Mikesell TD, Malcolm AE, Yang D, et al. A comparison of methods to estimate seismic phase delays: numerical examples for coda wave interferometry (Article) Geophys J Int 2015;202:347–60. https://doi.org/10.1093/gji/ggv138.
[90] Hughes DS, Kelly J. Second-order elastic deformation of solids. Phys Rev 1953;92:1145. https://doi.org/10.1103/PhysRev.92.1145.
[91] Toupin RA, Bernstein B. Sound waves in deformed perfectly elastic materials - Acoustoelastic effect (-&) J Acoust Soc Am 1961;33:216. https://doi.org/10.1121/1.1908623.
[92] Thurston R, Brugger K. Third-order elastic constants and the velocity of small amplitude elastic waves in homogeneously stressed media. Phys Rev 1964;133:A1604. https://doi.org/10.1103/PhysRev.133.A1604.
[93] Nogueira CL, Rens KL. Acoustoelastic Response of Concrete under Uniaxial Compression. Acids Mater J 2019;116:21–33. https://doi.org/10.14359/51714462.
[94] Zhang Y, Larose E, Moreau L, et al. Three-dimensional in-situ imaging of cracks in concrete using diffuse ultrasound. Struct Health Monit 2018;17:279–84. https://doi.org/10.1177/1475921717690938.
[95] Sutton MA, Orteu JJ, Schreier HW. Image Correlation for Shape, Motion and Deformation Measurements: Basic Concepts, Theory and Applications. New York: Springer; 2009. https://doi.org/10.1007/978-0-387-78747-3.
[96] Pan B, Qian K, Xie H, et al. Two-dimensional digital image correlation for in-plane displacement and strain measurement: a review. Meas Sci Technol 2009;20:062001. https://doi.org/10.1088/0957-0233/20/6/062001.
[97] Alqurashi I, Alver N, Bagci U, et al. A review of ultrasonic testing and evaluation methods with applications in civil NDT/E. J Nondestruct Eval 2025;44:53. https://doi.org/10.1007/s10921-025-01190-0.
[98] Mao S, Mordret A, Campillo M, et al. On the measurement of seismic traveltime changes in the time-frequency domain with wavelet cross-spectrum analysis. Geophys J Int 2020;221:550–68. https://doi.org/10.1093/gji/ggz495.
[99] Dumoulin C, Deraemaeker A. All-season monitoring of concrete repair in an urban tunnel in Brussels using embedded ultrasonic transducers with emphasis on robustness to environmental variations. J Civ Struct Health Monit 2021;11:879–95. https://doi.org/10.1007/s13349-021-00486-9.
[100] Cheng H, Yang Y, Besseling F, et al. Monitoring the Concrete Slab Bridge on Balladelaan in the Netherlands using Embedded Ultrasonic Sensors. IABSE Congress Ghent 2025: The Essence of Structural Engineering for Society. International Association for Bridge and Structural Engineering (IABSE); 2025. p. 1549–57.
[101] Lantsoght E, van der Veen C, de Boer A, et al. Proof load testing of reinforced concrete slab bridges in the Netherlands. Struct Concr 2017;18:597–606. https://doi.org/10.1002/suco.201600171.
[102] Lantsoght EO, van der Veen C, Hordijk DA, et al. Development of recommendations for proof load testing of reinforced concrete slab bridges. Eng Struct 2017;152:202–10. https://doi.org/10.1016/j.engstruct.2017.09.018.
[103] Lantsoght EO, Yang Y, Van der Veen C, et al. Stop criteria for flexure for proof load testing of reinforced concrete structures. Front Built Environ 2019;5:47. https://doi.org/10.3389/fbuil.2019.00047.
[104] Liu C, Dobson J, Cawley P. Efficient generation of receiver operating characteristics for the evaluation of damage detection in practical structural health monitoring applications. Proc R Soc A Math Phys Eng Sci 2017;473:20160736. https://doi.org/10.1098/rspa.2016.0736.
[105] Giglioni V, García-Macías E, Venanzi I, et al. The use of receiver operating characteristic curves and precision-versus-recall curves as performance metrics in unsupervised structural damage classification under changing environment. Eng Struct 2021;246:113029. https://doi.org/10.1016/j.engstruct.2021.113029.
[106] Jahangiri M, Palermo A, Kamali S, et al. A procedure to estimate the minimum observable damage in truss structures using vibration-based structural health monitoring systems. Probabilistic Eng Mech 2023;73:103451. https://doi.org/10.1016/j.probengmech.2023.103451.
[107] Kazemi F, Shafighfard T, Jankowski R, et al. Active learning on stacked machine learning techniques for predicting compressive strength of alkali-activated ultra-high-performance concrete. Arch Civ Mech Eng 2024;25:24. https://doi.org/10.1007/s43452-024-01067-5.
[108] Shafighfard T, Kazemi F, Asgarkhani N, et al. Machine-learning methods for estimating compressive strength of high-performance alkali-activated concrete. Eng Appl Artif Intell 2024;136:109053. https://doi.org/10.1016/j.engappai.2024.109053.
[109] Sun Y, Cheng H, Zhang S, et al. Prediction & optimization of alkali-activated concrete based on the random forest machine learning algorithm. Constr Build Mater 2023;385:131519. https://doi.org/10.1016/j.conbuildmat.2023.131519.